Application of symmetric instability parameterization in the Coastal and Regional Ocean Community Model (CROCO)

Jihai Dong[1], Baylor Fox-Kemper[2], Jinxuan Zhu[2], and Changming Dong[1]

[1]Nanjing University of Information Science and Technology
[2]Brown University

November 26, 2022

Abstract

As one kind of submesoscale instability, symmetric instability (SI) of the ocean surface mixed layer (SML) plays a significant role in modulating the SML energetics and material transport. The small spatial scales of SI, $O(10 \text{ m} \sim 1 \text{ km})$, are not resolved by current climate ocean models and most regional models. This paper describes comparisons in an idealized configuration of the SI parameterization scheme proposed by Bachman et al. (2017) (SI-parameterized) versus the K-Profile Parameterization (KPP) scheme (SI-neglected run) as compared to a SI-permitting model; all variants use the Coastal and Regional Ocean Community Model version of the Regional Ocean Modeling System (CROCO-ROMS) and this paper also serves to introduce the SI parameterization in that model. In both the SI-parameterized and SI-permitting model, the geostrophic shear production is enhanced and anticyclonic potential vorticity is reduced versus the SI-neglected model. A comprehensive comparison about the energetics (geostrophic shear production, vertical buoyancy flux), mixed layer thickness, potential vorticity, and tracer redistribution indicates that all these variables in the SI-parameterized case have structures closer to the SI-permitting case in contrast to the SI-neglected one, demonstrating that the SI scheme has a positive improvement to capture the impacts of SI. This work builds toward applying the SI scheme in a regional or climate model.

Application of symmetric instability parameterization in the Coastal and Regional Ocean Community Model (CROCO)

Jihai Dong[1,2], Baylor Fox-Kemper[3], Jinxuan Zhu[3] and Changming Dong[1,2]

[1]School of Marine Sciences, Nanjing University of Information Science and Technology, Nanjing, Jiangsu, China.

[2]Southern Marine Science and Engineering Guangdong Laboratory (Zhuhai), Zhuhai, Guangdong, China.

[3]Department of Earth, Environmental, and Planetary Sciences, Brown University, Providence, Rhode Island, USA.

Corresponding author: Changming Dong (cmdong@nuist.edu.cn)

Key Points:

- A symmetric instabilitiy parameterization scheme is implemented in the CROCO

- The impacts of symmetric instability are evaluated based on three comparison simulations with different spatial resolutions

- The scheme captures the impacts of symmetric instability and improves the model simulation results

19   **Abstract**

20   As one kind of submesoscale instability, symmetric instability (SI) of the ocean surface mixed
21   layer (SML) plays a significant role in modulating the SML energetics and material transport.
22   The small spatial scales of SI, $O(10 \text{ m} \sim 1 \text{ km})$, are not resolved by current climate ocean models
23   and most regional models. This paper describes comparisons in an idealized configuration of the
24   SI parameterization scheme proposed by Bachman et al. (2017) (SI-parameterized) versus the K-
25   Profile Parameterization (KPP) scheme (SI-neglected run) as compared to a SI-permitting model;
26   all variants use the Coastal and Regional Ocean Community Model version of the Regional
27   Ocean Modeling System (CROCO-ROMS) and this paper also serves to introduce the SI
28   parameterization in that model. In both the SI-parameterized and SI-permitting model, the
29   geostrophic shear production is enhanced and anticyclonic potential vorticity is reduced versus
30   the SI-neglected model. A comprehensive comparison about the energetics (geostrophic shear
31   production, vertical buoyancy flux), mixed layer thickness, potential vorticity, and tracer
32   redistribution indicates that all these variables in the SI-parameterized case have structures closer
33   to the SI-permitting case in contrast to the SI-neglected one, demonstrating that the SI scheme
34   has a positive improvement to capture the impacts of SI. This work builds toward applying the SI
35   scheme in a regional or climate model.

36   **Plain Language Summary**

37   Symmetric instability (SI) of the ocean surface mixed layer has spatial scales of tens of meters to
38   kilometers, playing a significant role in ocean energy transfer and material transport. The coarse
39   resolution of current climate and regional models cannot resolve SI due to its small scales, so its
40   impacts require to be parameterized. This work impliments a SI parameterization scheme in the
41   Coastal and Regional Ocean Community Model (CROCO) and the evalution indicates that the
42   scheme improves the simulation results to capture the SI impacts. The work suggests a potential
43   application of the sheme in a reginoal or climate model.

44   **1 Introduction**

45   Physical processes in the ocean surface mixed layer (SML) modulate the SML, impacting
46   the energy budget of global ocean and thereby climate change. With spatial scales far from being
47   resolved by climate ocean models (from tens of meters to kilometers), parameterizations of SML
48   processes including surface waves, Langmuir circulation and submesoscale currents are a key
49   avenue to improve climate and weather models (e.g., Fox-Kemper et al., 2008; Fox-Kemper et
50   al., 2011; Noh et al., 2016; Qiao et al., 2016; Li et al., 2016). Among these processes,
51   submesoscale instabilities can enhance vertical transports (e.g., Boccaletti et al., 2007; Lévy et
52   al., 2012; Su et al., 2018), and energy cascades (e.g., Capet et al., 2008a; Buckingham et al.,
53   2019; Dong et al., 2020a), which are dynamics requiring parameterization in ocean models.

54   The submesoscale consists of those processes with Rossby and Richardson numbers
55   around $O(1)$ (i.e., Ro ~ 1, Ri ~ 1) imparting time scales of hours to O(1) day and lengths of tens
56   of meters to O(10) km (Thomas et al., 2008; McWilliams, 2016). Observations and simulations
57   find submesoscales are ubiquitous over the globe (Callies et al., 2015; Buckingham et al., 2016;
58   Su et al., 2018) and vertically over full water depth (Molemaker et al., 2015; Gula et al., 2016;
59   Siegelman et al., 2019; de Marez et al., 2020). The SML is the layer of greatest submesoscale
60   activity. Symmetric instability (SI) is a classical submesoscale instability, in that it requires
61   rotation and some density variation, and it partially accounts for the SML submesoscale activity

62 (D'Asaro et al., 2011; Thomas et al., 2013; Thompson et al., 2016; Buckingham et al., 2019; Yu
63 et al., 2019; Wenegrat et al., 2020).

64 In the SML, the Ertel potential vorticity (PV),

$$q = (f\mathbf{k} + \nabla \times \mathbf{v}) \cdot \nabla b, \tag{1}$$

66 is easily shifted toward anticyclonic values (i.e., opposite sign to local Coriolis parameter, *f*) at
67 fronts through weak vertical stratification and strong horizontal buoyancy gradients. Here,
68 $\nabla = \frac{\partial}{\partial x}\mathbf{i} + \frac{\partial}{\partial y}\mathbf{j} + \frac{\partial}{\partial z}\mathbf{k}$ is the three-dimensional gradient operator, $\mathbf{v}$ is the three-dimensional
69 velocity field, and $b = -g\rho/\rho_0$ is the buoyancy (g = 9.8 m s^{-2} is the gravitational
70 acceleration, ρ_0 = 1024 kg m^{-3} is the background seawater density). Anticyclonic PV favors SI
71 which is characterized by perturbation modes aligned along slanting isopycnals that feed on
72 geostrophic shear of fronts (Stone, 1966; Hoskins, 1974; Haine & Marshall, 1998; Haney et al.,
73 2015). The kinetic energy extracted by SI is transferred toward smaller scales and finally
74 supports local mixing enhancement in the SML (Taylor & Ferrari, 2010; D'Asaro et al., 2011;
75 Buckingham et al., 2019; Yu et al., 2019). SI also tends to restratify the SML, modulate the SML
76 thickness, and redistribute passive tracers (Bachman et al., 2017; hereinafter B17). Given that
77 fronts usually act as dynamical barriers to cross-front material transport, SI may be a significant
78 routine for lateral exchange across fronts (Wenegrat et al., 2020).

79 The fastest growing wavelength of SI in the SML with a uniform stratification *N* and
80 shear *U*/*H* (*U* is the velocity difference over the thickness of SI layer, *H*) can be estimated
81 through linear instability analysis as (Stone, 1966)

$$L_{SI} = \frac{U}{f}\sqrt{1 - Ri_b}. \tag{2}$$

83 Here, $Ri_b = \frac{N^2 f^2}{|\nabla_h b|^2}$ is the balanced Richardson number. In previous work, the authors (Dong et al.
84 2020b) use this relation to show that SI is expected to have spatial scales of O(10) m to O(1) km
85 over the global ocean, thus all current climate models and even submesoscale-permitting
86 regional models with resolutions of O(1) km are unable to directly resolve SI in most regions and
87 seasons. The results from Dong et al. (2020b) also indicate that SI is active in the SML globally
88 (in as much as 16% of wintertime regions) and potentially modulates the air-sea heat and
89 momentum exchanges (reducing the usable wind-work reduction by 11% globally). As a result,
90 the parameterization of SI in ocean models is expected to have a significant impact on simulation
91 accuracy and prediction capability.

92 The goal of this work is to implement the SI parameterization scheme proposed by B17
93 in the Coastal and Regional Ocean Community Model (CROCO) and evaluate the simulation
94 changes in terms of energetics, mixed layer thickness, potential vorticity and tracer redistribution
95 based on an idealized configuration of two fronts under surface forcing. The rest of the paper is
96 organized as follows: Section 2 introduces the theory of the SI parameterization and describes
97 the model setup; Section 3 assesses the SI scheme based on three comparison cases. The last
98 section discusses and concludes.

2 Symmetric instability parameterization and model setup

2.1 Symmetric instability parameterization

This section gives a brief description of the parameterization scheme that proposed by B17, although interested readers are referred to the greater detail of B17.

As SI can occur only when PV is anticyclonic, the SI layer, H is calculated as the depth below which fq_{bulk} becomes positive, which limits the deepest penetration depth of the unstable SI modes (Haney et al., 2015; Dong et al., 2020b),

$$fq_{bulk} = f\left(f\Delta b + \langle \zeta \rangle \Delta b + \Delta u \left\langle \frac{\partial b}{\partial y} \right\rangle - \Delta v \left\langle \frac{\partial b}{\partial x} \right\rangle \right) > 0. \tag{3}$$

Here, ζ is the vertical relative vorticity, Δ denotes the difference between the surface value and the value at a given depth, the angle bracket denotes a depth average over the same depth range. For a high-resolution model (such as the model used here), the vertical vorticity tends to be comparable to the local planetary vorticity, so we include the impacts of the vertical vorticity as suggested by Dong et al. (2020b) unlike the suggestion of B17.

As SI tend to mix and homogenize PV from the cyclonic values found in the stratified deeper layers into the anticyclonic region, surface forcing tending toward anticyclonic PV is necessary for sustained SI, called *forced* SI. The surface forcing driving anticyclonic PV injection (Thomas, 2005) includes sea surface heat and freshwater exchanges combined into the buoyancy forcing,

$$B_0 = B_T + B_S = g\alpha \frac{Q_{net\_heat}}{\rho_0 C_P} + g\beta(EP)S \tag{4}$$

and the Ekman Buoyancy Flux driven by along-front wind at the surface,

$$EBF = \frac{\boldsymbol{\tau}_w \times \mathbf{k}}{\rho_0 f} \boldsymbol{\nabla}_h b. \tag{5}$$

Here, α is the thermal expansion coefficient, Q_{net_heat} is the net surface heat flux, $Cp = 4200$ J kg^{-1} $^{\circ}$C^{-1} is the seawater specific heat capacity, β is the saline contraction coefficient, EP is the net freshwater exchange due to evaporation and precipitation (the convection is for ocean loss of heat with positive Q_{net_heat} or freshwater with positive EP), and S is the sea surface salinity, and $\boldsymbol{\tau}_w$ is the wind stress. PV tends to be shifted toward anticyclonic values when $B_0 + EBF > 0$, i.e., toward convective destabilization. SI under $B_0 > 0$ and $EBF > 0$ have been studied using the Large Eddy Simulation (LES; e.g., Taylor & Ferrari, 2010; Thomas et al., 2013; Haney et al., 2015). The parameterization scheme proposed B17 relies heavily on forced SI for the rates of SI effects, combined with a condition that PV must be anticyclonic in order for the parameterization to be triggered.

The LES shows two distinct sublayers over the SI layer under $B_0 > 0$ and $EBF > 0$: a convective layer near the surface and a deeper SI-dominated layer below (e.g., Taylor & Ferrari, 2010). The relationship between the convective layer thickness, h, and the SI-layer, H, can be determined by a quartic equation (Thomas et al., 2013),

$$\left(\frac{h}{H}\right)^4 - c^3 \left(1 - \frac{h}{H}\right)^3 \left[\frac{w_*^3}{U^3} + \frac{u_*^2}{U^2} cos\theta_w\right]^2 = 0. \tag{6}$$

135 Here, $c = 14$ is an empirical constant, $w_* = (B_0 H)^{1/3}$ is the convective velocity by surface
136 buoyancy loss, $u_* = (|\boldsymbol{\tau}_w|/\rho_0)^{1/2}$ is the friction velocity, and θ_w is the angle between wind
137 vector and frontal current.

138 Once H and h are known, the geostrophic shear production (GSP) describing the kinetic
139 energy conversion rate to SI is parameterized as a piecewise linear function (Thomas et al.,
140 2013),

141
$$GSP = \begin{cases} 0 & ,z = 0 \\ F_{SI}\frac{z+H}{H} - B_0\frac{z+h}{h} & ,-h < z < 0 \\ F_{SI}\frac{z+H}{H} & ,-H < z < -h \\ 0 & ,z < -H \end{cases}, \tag{7}$$

142 where $F_{SI} = EBF + B_0$ (see further discussion in B17). A corresponding SI vertical viscosity
143 related to this kinetic energy extraction is calculated as,

144
$$\nu_{SI} = \frac{f^2}{|\nabla_h b|} GSP. \tag{8}$$

145 Assuming mixing takes on a simple form of the turbulent Prandtl number (i.e., $Pr = \frac{\nu_{SI}}{\kappa_{SI}}$), the
146 vertical diffusivity is calculated by

147
$$\kappa_{SI} = \frac{2\nu_{SI}}{1 + (10\max(0, Ri_b))^{0.8}}. \tag{9}$$

148 As mentioned in the preceding section, the overturning cells of SI can redistribute passive tracers
149 isopycnally. This flux is accomplished by an along-isopycnal scalar diffusivity,

150
$$K_{SI} = \frac{GSP}{f^2}\min(1, Ri_b{}^2). \tag{10}$$

151 This along-isopycnal diffusivity is represented by a symmetric tensor in Redi (1982) form in the
152 z-coordinate, which can be written as,

153
$$\mathbf{K}_{SI} = \frac{K_{SI}}{b_x^2 + b_y^2 + b_z^2}\begin{bmatrix} b_y^2 + b_z^2 & -b_x b_y & -b_x b_z \\ -b_x b_y & b_x^2 + b_z^2 & -b_y b_z \\ -b_x b_z & -b_y b_z & b_x^2 + b_y^2 \end{bmatrix}. \tag{11}$$

154 In the CROCO, this along-isopycnal mixing is easily added via the built-in lateral tracer mixing
155 along isopycnal surface algorithms.

156 As recommended by B17, the SI parameterization should be implemented alongside
157 another default boundary layer turbulence closure, such as the nonlocal K-Profile
158 Parameterization (KPP; Large et al., 1994) scheme used here, so that when the SI conditions are
159 not met and SI is stable the other scheme is used. In practice, this means that the SI scheme is
160 active only within frontal regions under destabilizing surface forcing. As the default turbulence
161 scheme calculates momentum and tracer fluxes related to mixing, the SI scheme will be activated
162 only when $B_0 > 0$ and $EBF > 0$ and $h < 0.95H$ (a convenient threshold value for SI activity,
163 otherwise SI is dominated by convection). When the SI scheme is activated, the vertical fluxes,
164 F_{wC} for tracers with nonzero surface fluxes in the convective layer needs to be considered, which
165 can be parameterized as a linear profile,

166
$$F_{wC} = \begin{cases} 0 & ,z = 0 \\ F_0 \dfrac{z+h}{h} & ,-h < z < 0. \\ 0 & ,z < -h \end{cases} \qquad (12)$$

167 Here, F_0 is the surface flux for a given tracer, C. We note that in both (7) and (12), the surface
168 flux boundary condition is set to zero—this choice is necessary to ensure conservation of
169 properties exchanged between the atmosphere and ocean: the SI scheme is designed to affect
170 distributions within the SML, not the air-sea fluxes (although we will revisit this in the context of
171 the SI-permitting runs later).

172   Finally, the momentum and tracer equations that include all these SI terms in the *z*-
173 coordinate can be rewritten as,

174
$$\begin{cases} \dfrac{\partial u}{\partial t} + \mathbf{\nabla} \cdot (\mathbf{v}u) - fv = -\dfrac{\partial \phi}{\partial x} + \dfrac{\partial}{\partial z} v_{SI} \dfrac{\partial u}{\partial z} + \mathcal{F}_u + \mathcal{D}_u \\ \dfrac{\partial v}{\partial t} + \mathbf{\nabla} \cdot (\mathbf{v}v) + fu = -\dfrac{\partial \phi}{\partial y} + \dfrac{\partial}{\partial z} v_{SI} \dfrac{\partial v}{\partial z} + \mathcal{F}_v + \mathcal{D}_v \\ \dfrac{\partial C}{\partial t} + \mathbf{\nabla} \cdot (\mathbf{v}C) = \dfrac{\partial}{\partial z} v_{SI} \dfrac{\partial u}{\partial z} + \mathbf{\nabla} \cdot (\mathbf{K}_{SI}C) - \dfrac{\partial F_{wC}}{\partial z} + \mathcal{F}_C + \mathcal{D}_C \end{cases} . \qquad (13)$$

175 Here, $\mathbf{\nabla} = \dfrac{\partial}{\partial x}\mathbf{i} + \dfrac{\partial}{\partial y}\mathbf{j} + \dfrac{\partial}{\partial z}\mathbf{k}$ is the three-dimensional gradient operator, $\mathbf{v}$ is the three-
176 dimensional velocity field, ϕ is the pressure potential, $\mathcal{F}$ and $\mathcal{D}$ are the corresponding forcing
177 and horizontal diffusive terms, respectively. In this work, we will apply the SI scheme alongside
178 the KPP as recommended by B17.

179   Steps to apply SI scheme in the CROCO are summarized as follows:

180   1) the momentum and tracer fluxes are calculated by the KPP;

181   2) then the surface bulk PV, q_{bulk} is calculated from the model fields and Equation (3),
182 and the surface buoyancy flux, B_0, and the surface Ekman buoyancy flux, EBF are calculated
183 from the surface fluxes in Equation (4−5);

184   3) For those grid points with $fq_{bulk} < 0$, $B_0 > 0$ and $EBF > 0$, the SI layer H is
185 calculated based on Equation (3) and then the convective layer h can be determined by Equation
186 (6);

187   4) If $\dfrac{h}{H} < 0.95$, the SI scheme is activated, and momentum and tracer fluxes are
188 calculated to replace the values from the KPP using Equation (7−13). The CROCO uses the
189 terrain-following coordinate (i.e., sigma-coordinate) system and details of introducing the sigma-
190 coordinate and grid discretization can be referred to Chapter 3−4 of Hedström (2009).

191   2.2 Model setup

192   The parameterization and simulation are built with the CROCO (http://www.croco-
193 ocean.org). The CROCO is a new model built upon the ROMS-Agrif (Jullien et al., 2019). The
194 simulation in this work is still accomplished under the hydrostatic approximation.

195   An idealized model is established with a domain of 65 km × 65 km × 150 m (Figure 1).
196 There are 60 layers in the vertical with finer resolution concentrated in the SML. The
197 background state of the model has a constant salinity $S = 35$ PSU, and a vertical potential
198 temperature profile as follows,

199
$$\theta\,(\text{°C}) = \begin{cases} 20 & ,-50 \leq z \leq 0 \\ 20 + 0.02(z + 50), & -150 < z < -50 \end{cases}. \tag{14}$$

200 This profile provides a SML above 50 m and a thermocline below (Figure 1b). This linear
201 thermocline profile yields a buoyancy frequency in the stratified interior of $75f$. Based on the
202 background temperature profile, two y-direction fronts in the SML with a horizontal scale of 3
203 km and a temperature difference of 0.3 °C are initialized at the beginning, yielding horizontal
204 buoyancy gradients of $5.3f$. A constant Coriolis parameter equivalent to a latitude of 35° is
205 chosen ($f=8.4\times10^{-5}\,\text{s}^{-1}$). Given the mixed layer depth of 50 m, this temperature difference and
206 horizontal scale roughly match the mixed layer depth dynamically expected after geostrophic
207 adjustment, i.e., the fronts are roughly one deformation radius wide when the boundary layer
208 stratification is $28f$. Meanwhile, a constant northward wind stress, $\tau = 0.03\,\text{N m}^{-2}$ and a surface
209 net heat flux with a diurnal cycle, $Q = 20\sin(2\pi T)\,\text{W m}^{-2}$ (T starts from 0 in days) are applied
210 in the simulation. The heat flux here is much weaker (about one order of magnitude smaller)
211 compared with the realistic one, chosen to favor a thick SI-dominated layer. In direction, the
212 wind is in a downfront direction for the left front with a northward geostrophic current in Figure
213 1 (hereinafter NFront) and thus destabilizing but upfront for the right front with a southward
214 geostrophic current (hereinafter SFront) and thus restratifying. A comparison between the two
215 fronts will highlight frontal instabilities due to the downfront wind and EBF. The horizontal
216 viscosity is chosen as $5\,\text{m s}^{-2}$. Periodic boundary conditions are used in the simulation. The
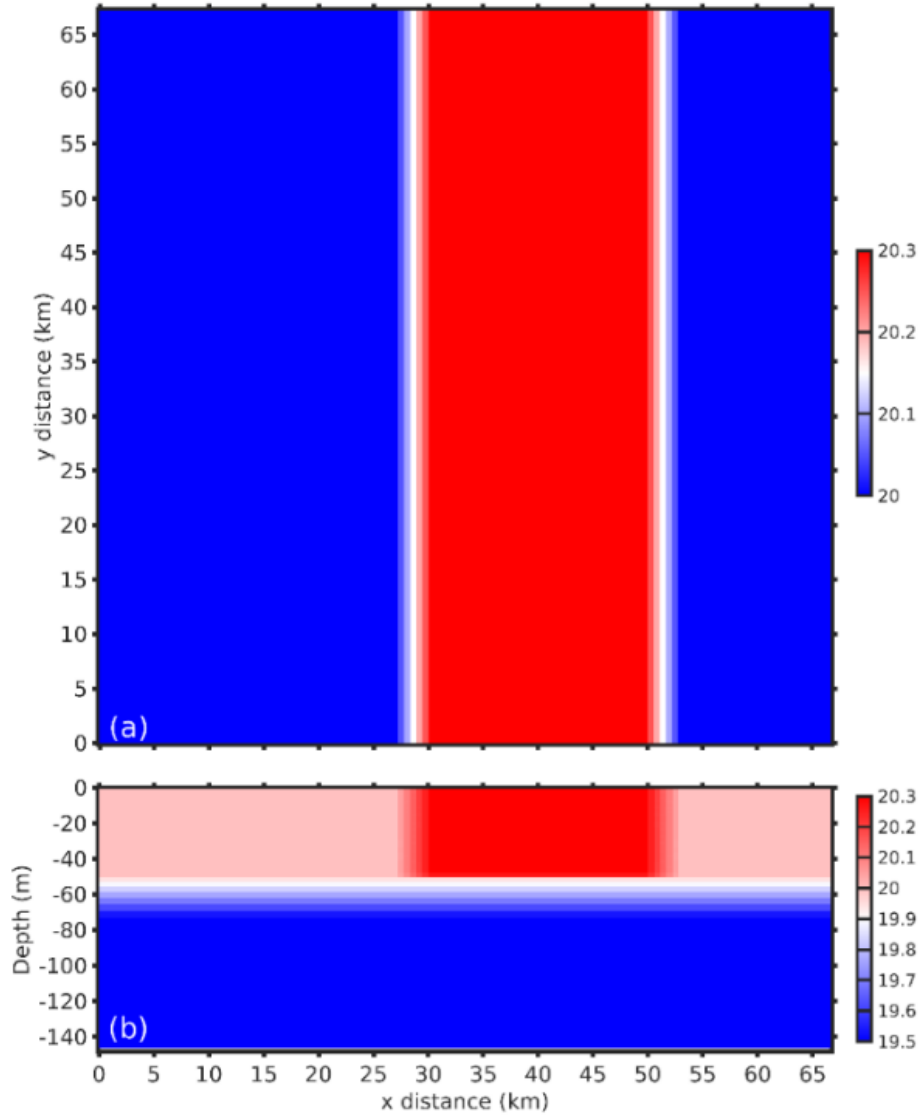217 simulation lasts for 20 days. Details about the model configurations are listed in Table 1.

218
219   Figure 1 Potential temperature fields (^{o}C) in (a) the horizontal plane at the surface and (b)
220   transverse plane in x direction.

221

222   Based on Equation (2), SI tends to have spatial scales about 0.5 ~ 1.5 km at the fronts
223 during geostrophic adjustment with $0.25 \leq Ri_b \leq 0.95$. As a result, three comparison cases are
224 conducted:

225 (1) **KPP550**: this case has a coarse spatial resolution of 550 m and the vertical mixing is
226   accomplished solely by the KPP scheme;

227 (2) **SI550**: this case has a coarse spatial resolution of 550 m and the SI scheme is activated
228   alongside the default KPP scheme;

229 (3) **KPP55**: this case has a high spatial resolution of 55 m with the KPP scheme, which is
230   intended to resolve SI directly (partially resolved, see the discussion section). According to
231   Bachman & Taylor (2014), the impacts of SI are only partially accomplished in a model that

232   partially resolves SI due to coarse resolution or large horizontal viscosity, yielding qualitative
233   but not quantitative agreement. A discussion of the potential impacts from resolution
234   limitations and the hydrostatic approximation follows the results.

235
236   Table 1 Model configurations of the different cases.

Parameter	Case		
	KPP550	SI550	KPP55
Domain size	65 km × 65 km × 150 m	65 km × 65 km × 150 m	65 km × 65 km × 150 m
Horizontal Resolution	550 m	550 m	55 m
Vertical layers	60	60	60
Initial SML depth	50 m	50 m	50 m
Front scale	3 km	3 km	3 km
Temperature difference	0.3 $^{\circ}$C	0.3 $^{\circ}$C	0.3 $^{\circ}$C
Horizontal buoyancy gradient	5.3f	5.3f	5.3f
Thermocline stratification	75f	75f	75f
Surface wind stress	0.03 N m^{-2}	0.03 N m^{-2}	0.03 N m^{-2}
Heat flux	20 W m^{-2}	20 W m^{-2}	20 W m^{-2}
Coriolis parameter	8.4×10^{-5} s^{-1}	8.4×10^{-5} s^{-1}	8.4×10^{-5} s^{-1}
Horizontal viscosity	5 m s^{-2}	5 m s^{-2}	5 m s^{-2}
Turbulence scheme	KPP	SI+KPP	KPP

237

238   A similar two-front setup has been used to investigate submesoscale instabilities,
239 including interactions with Langmuir turbulence (Hamlington et al., 2014), impacts on tracer
240 transports (Smith et al., 2016), and the application of the SI scheme in the MIT general
241 circulation model (Zhu, 2017). As the fronts evolve, different frontal instabilities occur and two
242 notable instabilities are mixed layer instabilities (MLI; Boccaletti et al., 2007; Fox-Kemper et al.,
243 2008) and SI (Hoskins, 1974; Taylor & Ferrari, 2010; Thomas et al., 2013; B17), which are the
244 typical submesoscale instabilities that occur along fronts in the absence of strain (Haine &
245 Marshall, 1998; Haney et al., 2015). The spatial resolution of the coarse-resolution cases can
246 resolve MLI but hardly SI, while the resolution of the high-resolution case is supposed to resolve
247 both MLI and SI. Neither resolution resolves convective boundary layer turbulence, nor would
248 this be accurately modeled in a hydrostatic system, so even in the high-resolution simulation the
249 KPP is used.

250 **3 Results**

251   3.1 Symmetric instability in KPP55 and primary comparison

252   Acting as a "truth" case, the SI-resolving or SI-permitting degree of the high-resolution
253   case (i.e., KPP55) needs to be clarified (Bachman & Taylor, 2014). To compare this high-
254   resolution run against the coarser runs, a highpass filter with a cutoff scale of 1 km is applied on
255   the velocity fields in KPP55. The chosen cutoff scale is near the Nyquist sampling rate of the
256   coarse-resolution cases, indicating that the velocity perturbations retained after the filter is
257   applied are not resolved by the coarse-resolution cases (i.e., KPP550 and SI550). The
258   instantaneous transverse sections of PV and the cross-front (i.e., x-direction) velocity
259   perturbations are investigated (Figure 2; Figure 3; Figure 4). The surface net heat flux at 9.25
260   days is negative and thus heats the ocean, leading to vertical restratification and positive PV for
261   most regions (Figure 2a). Weak negative PV values can still be observed between 20 ~ 50 m, a
262   residual of the previous nighttime cooling. The only exception is at the location of the EBF-
263   destabilized front (i.e., NFront), where strong negative PV values occupy the whole SML as a
264   result of the strong horizontal buoyancy gradients and vertical shear (Equation (2-3)). The SI
265   layer thickness calculated based on the bulk PV is negligible everywhere but quite thick at the
266   frontal regions where this negative PV is present (yellow line in Figure 2a). Precisely occupying
267   the region of negative PV, remarkable alternating cross-front velocity perturbations typical of SI
268   concentrating around the NFront with magnitude up to 0.02 cm s^{-1} are observed (Figure 2b,
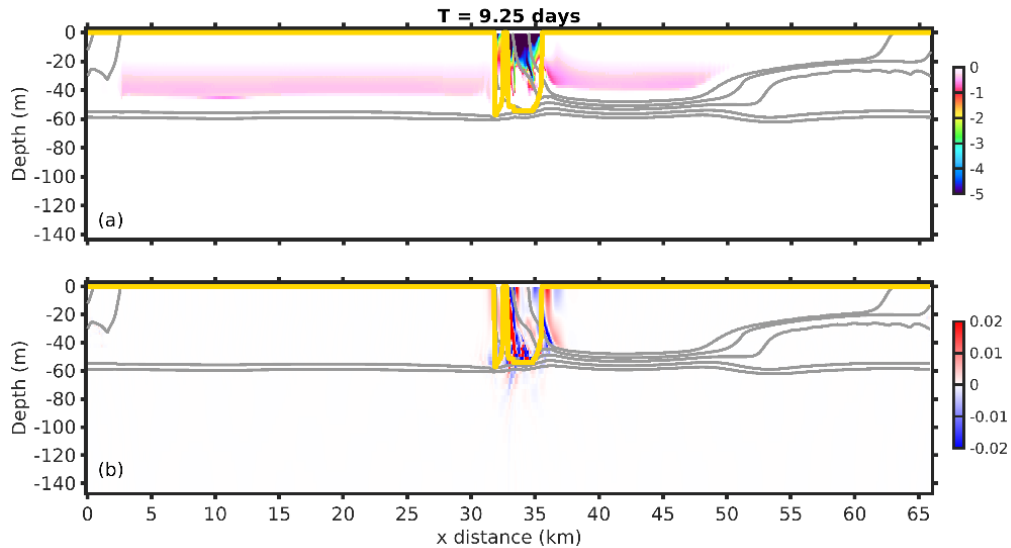269   Figure 4c).

270
271   Figure 2 Transverse sections of the instantaneous (a) PV ($\times 10^{-10}$ s^{-3}) and (b) cross-front velocity
272   perturbations (cm s^{-1}) at 9.25 days. The gray lines denote isolines of potential density, and the
273   yellow lines denote the SI layer thickness determined by Equation (3).

274

275   At 9.75 days, the net surface heat flux is positive (ocean cooling) with the maximum
276   magnitude, eroding the stratification and injecting negative PV. As a result, PV becomes
277   negative in the SML over most regions, except near the SFront where strong EBF-driven

278   stratification due to isopycnals is subject to Ekman overturning and flattening (Figure 3a).
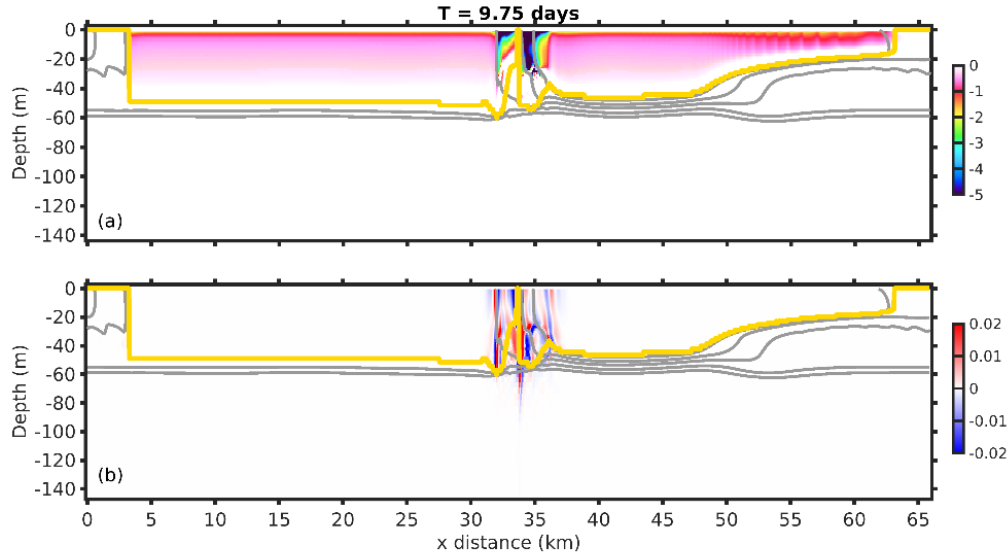279   Nevertheless, strong velocity perturbations are still observed only at NFront.

280
281   Figure 3 Transverse sections of the instantaneous (a) PV ($\times 10^{-10}$ s^{-3}) and (b) cross-front velocity
282   perturbations (cm s^{-1}) at 9.75 days. The gray lines denote isolines of potential density, and the
283   yellow lines denote the SI layer thickness from Equation (3).

284

285   Zooming in near the destabilized front indicates that the velocity perturbations are
286   dominated by along-isopycnal modes and mainly concentrate at the frontal regions with negative
287   PV (Figure 4): characteristics of SI (e.g., Bachman & Taylor, 2014; Haney et al., 2015). By 9.25
288   days, the region of SI activity is well characterized by the SI layer depth derived based on the
289   bulk PV equation (Figure 4a, c). Although the SI layer is deepened by surface cooling, the SI
290   modes at day 9.75 are still confined at the frontal region as a result of their extraction of
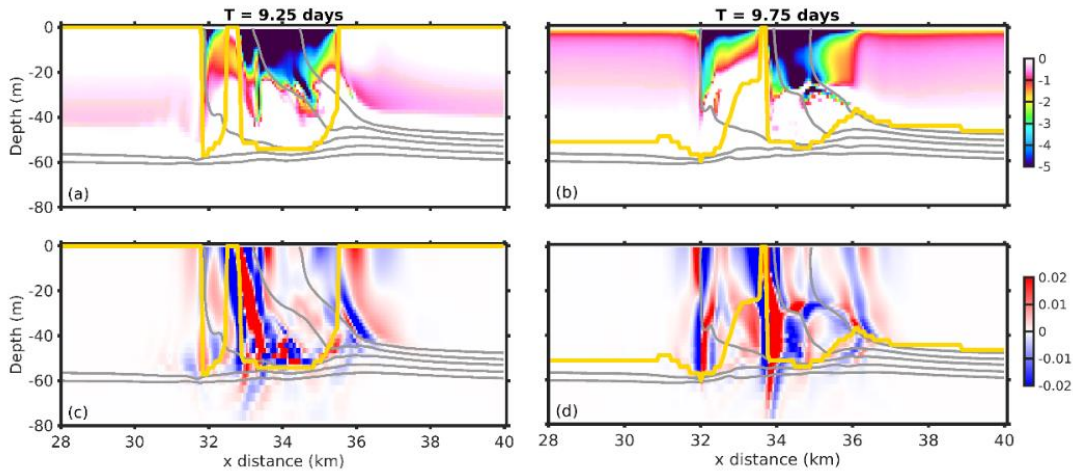291   geostrophic shear energy.

292
293   Figure 4 A zoom-in view on the transverse sections of (a, b) PV ($\times 10^{-10}$ s^{-3}) and (c, d) cross-front
294   velocity perturbations (cm s^{-1}) at NFront. The gray lines denote isolines of potential density, and
295   the yellow lines denote the SI layer thickness from Equation (3).

296
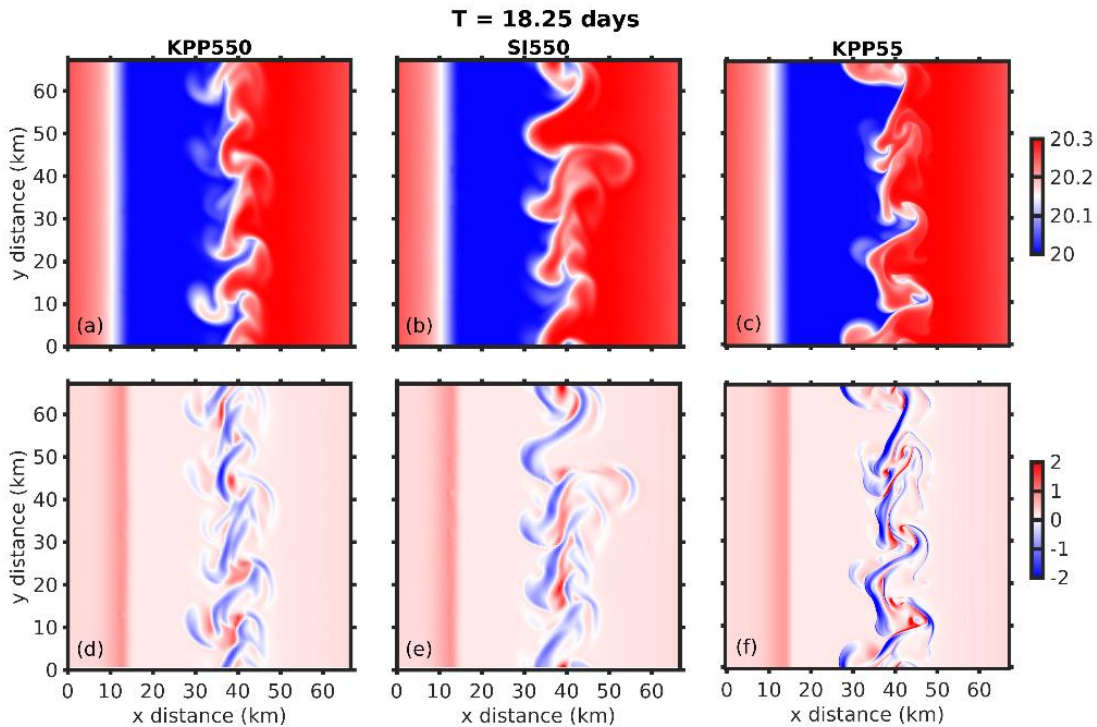
297   The three cases are first compared by examining the temperature and PV fields after 18
298 days—close to the end of simulation (Figure 5). The downfront wind strengthens the horizontal
299 gradients at NFront, making it sharper and more unstable and MLI generates meanders and
300 eddies, in contrast to SFront which is widened as it overturns (as seen in Hamlington et al.
301 (2014)). Figure 5 shows that active meanders and eddies are observed at NFront in both surface
302 temperature and PV from all three cases. The surface fluxes are warming the ocean at 18.25
303 days, so the surface PV is generally positive excepting the negative values at NFront. Despite the
304 diverse instability structures at the surface among these cases, the transverse sections of the
305 along-front averages reveal systematic differences reflecting SI impacts (Figure 6). The
306 temperature sections are similar in the three cases, showing a shallow SFront and a deep NFront.
307 The PV is similar at SFront but quite different at the three simulations' NFront. One expects MLI
308 at NFront to lead to potential energy release and mixed layer restratification (Boccaletti et al.,
309 2007). Thus, at NFront the mixed layer depth is shoaled by MLI and positive PV intrudes to
310 shallow depth above 20 m in all three simulations. However, compared with KPP550, the
311 positive PV intrudes to a shallower depth in SI550 and KPP55 (Figure 6d, e, f), a result of the SI
312 transport of stratified water into the mixed layer. Correspondingly, the KPP boundary layer
313 depths, H_{KPP} determined by a critical bulk Richardson number of 0.3 (Large et al., 1994) is
314 shallower at the fronts in the SI550 and KPP55 cases (gray lines in Figure 6d, e, f).

315
316   Figure 5 Surface distributions of the instantaneous (a, b, c) temperature (^{o}C) and (d, e, f) PV
317 ($\times 10^{-9}$ s^{-3}) at 18.25 days. The left, middle and right columns are results from KPP550, SI550 and
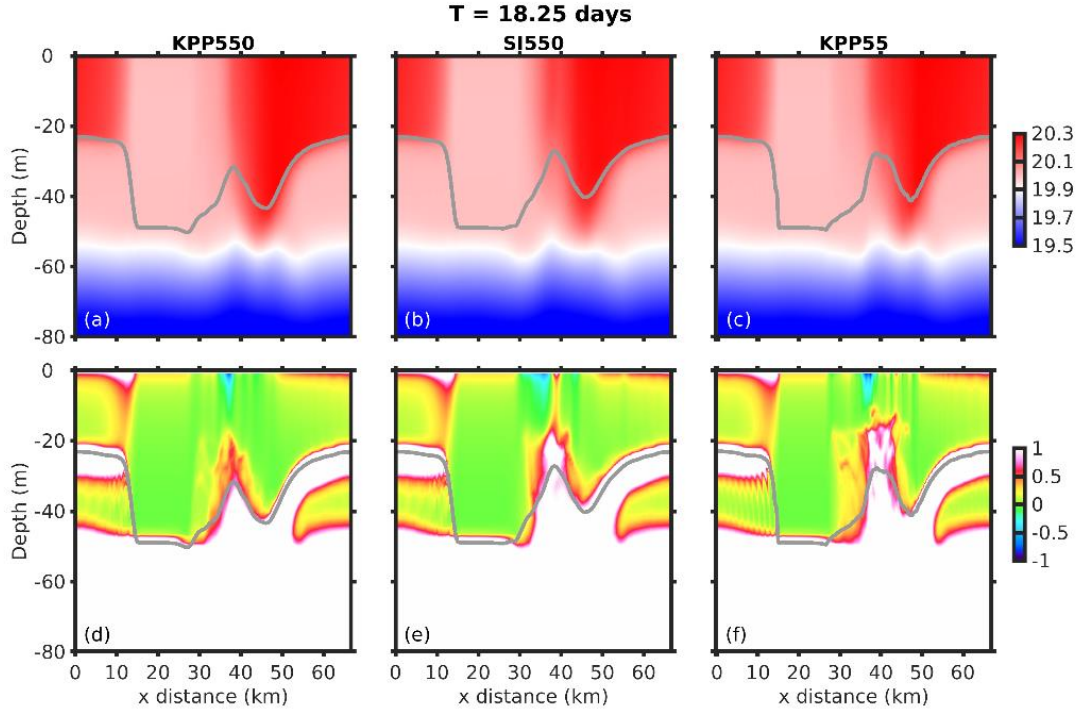318   KPP55, respectively.

Figure 6 Transverse sections of the y-direction averaged (a, b, c) temperature (^{o}C) and (d, e ,f) PV ($\times 10^{-9}$ s^{-3}) at 18.25 days. The gray lines denote the KPP boundary layer depth. The left, middle and right columns are results from KPP550, SI550 and KPP55, respectively.

At 18.75 days, the intensified surface cooling results in negative PV in the SML, but the strongest negative PV is still at NFront (Figure 7). B_0 and *EBF* are both cooling at the NFront at this time, and the derived SI layer depth H and convective layer depth h are shown (purple and black lines in Figure 8). These three depths (including H_{KPP}) overlap at most regions, but are distinct at NFront, consistent with the expectation of SI effects there in SI550 and the realization of SI effects in KPP55. The convective layer is shallower than the KPP boundary layer depths, while the SI layer is deeper (per B17).

Overall, when the SI parameterization is included, the KPP boundary layer and SI layer both become shallower due to the specified restratification by SI, which is closer to the high-resolution simulation result in KPP55, compared with the coarse-resolution case KPP550 which does not parameterize any restratification. SI dominates below the convective layer depth and the mechanism for restratification is SI-driven exchange of stratified thermocline water by SI between the SML and the deeper layers near H compared with the KPP550 result which has limited parameterized effect below H_{KPP}.
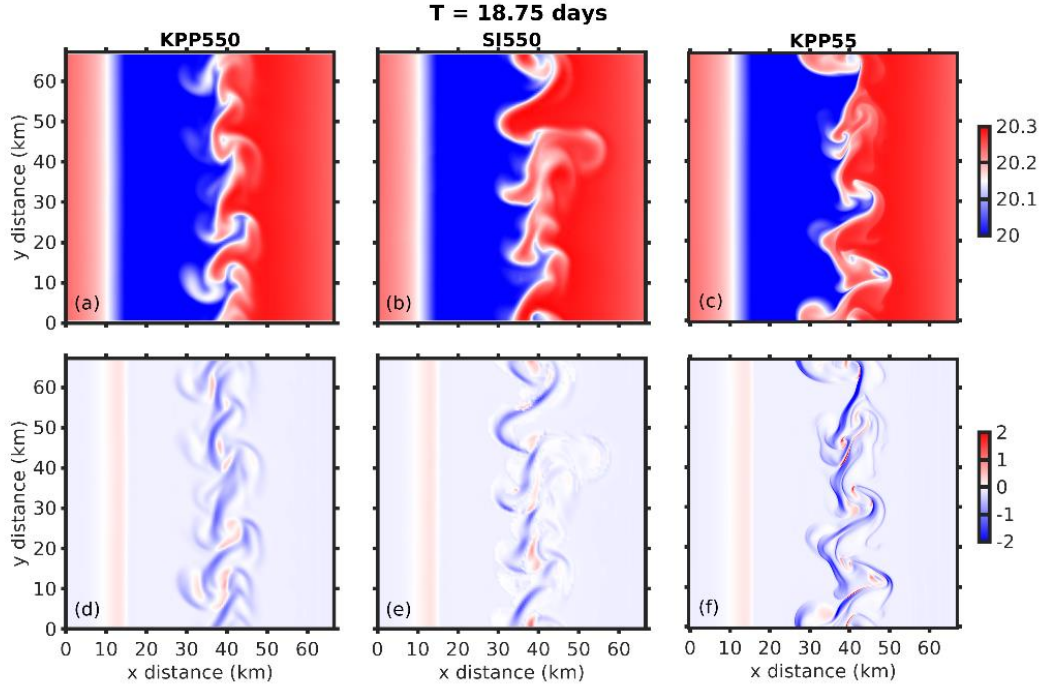
Figure 7 Surface distributions of the instantaneous (a, b, c) temperature (^{o}C) and (d, e, f) PV ($\times 10^{-9}$ s^{-3}) at 18.75 days. The left, middle and right columns are results from KPP550, SI550 and KPP55, respectively.
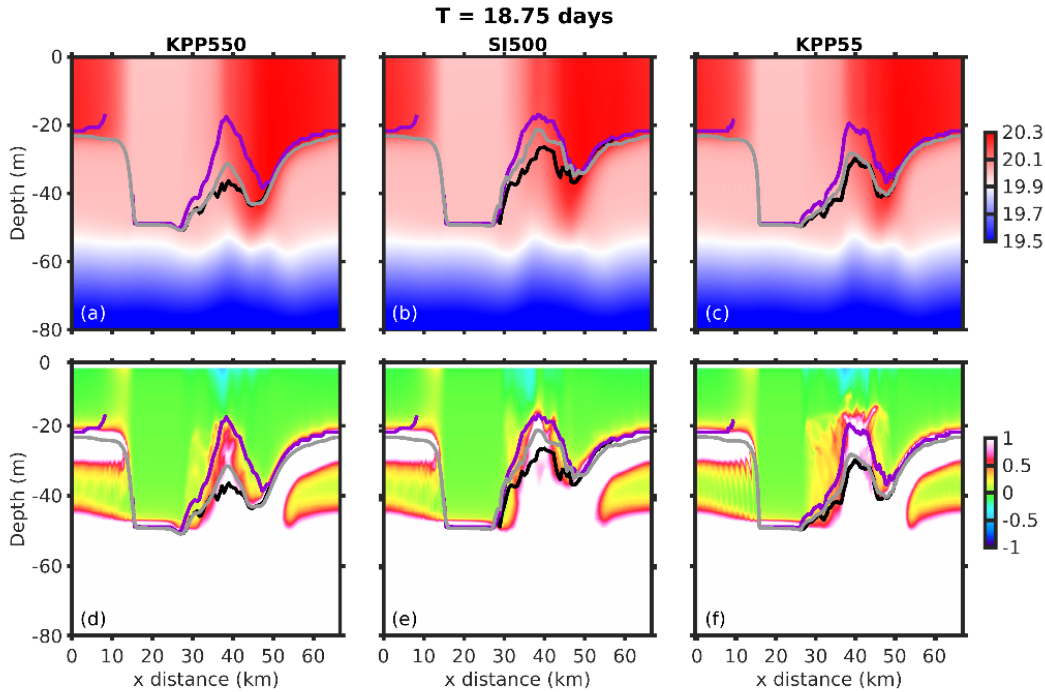

Figure 8 Transverse sections of the y-direction averaged (a, b, c) temperature (^{o}C) and (d, e ,f) PV ($\times 10^{-9}$ s^{-3}) at 18.75 days. The purple, gray and black lines denote the convective layer depth (h), KPP boundary layer depth (H_{KPP}) and SI layer depth (H), respectively. The left, middle and right columns are results from KPP550, SI550 and KPP55, respectively.

347

348   3.2 Energetics

349   Fundamentally, energetics analysis is useful for assessing the effects of the SI
350   parameterization scheme, as SI grows by extracting the geostrophic kinetic energy of frontal
351   currents. To assess these three cases, the velocity, temperature and buoyancy fields are
352   decomposed into the background, MLI and SI components, namely,

353
$$\begin{cases} \mathbf{u} = \mathbf{u}_b + \mathbf{u}' = \mathbf{u}_b + \mathbf{u}_{MLI} + \mathbf{u}_{SI} \\ w = w_b + w' = w_b + w_{MLI} + w_{SI} \\ \theta = \theta_b + \theta' = \theta_b + \theta_{MLI} + \theta_{SI} \\ b = b_b + b' = b_b + b_{MLI} + b_{SI} \end{cases}. \tag{15}$$

354   Here, the background component is calculated by whole-domain averaging in the along-front
355   direction (i.e., y-direction), the SI component is calculated by a highpass filter with a cutoff scale
356   of 1 km (this scale is just below the scale that the coarse-resolution cases can resolve, so the SI
357   component is expected to be zero for those cases), and the MLI component is the residual after
358   removing these large and small scale components. The background horizontal velocity
359   component is further decomposed into the geostrophic and Ekman/ageostrophic components,
360   $\mathbf{u}_b = \mathbf{u}_g + \mathbf{u}_E$. The geostrophic component is determined based on the thermal wind balance
361   ($f\mathbf{k} \times \frac{\partial \mathbf{u}_g}{\partial z} = -\nabla_h b_b$; note there is only v_g and u_g should be zero based on this calculation).

362   Based on the decomposition, the GSP is calculated as (with overbar denoting horizontal
363   averages, and the whole equation is calculated as an integral over the horizontal),

364
$$GSP = K_v (\frac{\partial \mathbf{u}_g}{\partial z})^2 - \overline{\mathbf{u}'w'} \frac{\partial \mathbf{u}_g}{\partial z}, \tag{16}$$

365   where K_v is the model output vertical viscosity, noting that in the coarse-resolution simulations
366   this viscosity is intended to capture the full GSP by SI (B17). The vertical buoyancy flux is
367   evaluated in two contributions: the vertical buoyancy flux, BF related to vertical diffusivity and
368   SI (parameterized or resolved) and the vertical buoyancy production, BP, related to potential
369   energy release due to MLI. The BF is calculated as,

370
$$BF = -g\alpha K_t \left(\frac{\partial \theta_b}{\partial z} - \gamma_\theta \right) \tag{17}$$

371   in KPP550,

372
$$BF = -g\alpha K_t \left(\frac{\partial \theta_b}{\partial z} - \gamma_\theta \right) + w_{SI} b_{SI} \tag{18}$$

373   in KPP55 and

374
$$BF = -K_t N^2 + g\alpha F_{w\theta} \tag{19}$$

375   in SI550. Here, K_t is the model output vertical diffusivity, γ_θ is the nonlocal heat transport term
376   (Large et al., 1994), and $F_{w\theta}$ is the vertical heat convection determined by Equation (12) for the
377   parameterized SI tracer transport. Note that the along-isopycnal transport of buoyancy is zero, by
378   the rotated diffusion (Redi, 1982) formulation of Equation (11). The BP is calculated for the MLI
379   contribution as

380
$$BP = w_{MLI} b_{MLI} \tag{20}$$

381   in all the three cases.

382   The vertical profiles of the horizontally-averaged GSP, BF and BP calculated over
383   NFront (considering the fronts moves from west to east, a x-direction 30-km range covering the
384   front is chosen for averaging and the same below) during times of cooling (positive surface heat
385   flux to trigger the SI parameterization) over simulation days 8 through 12 are shown in Figure 9.
386   The calculated GSP in all three cases is nearly zero below the SML and positive in the SML,
387   implying an extraction of energy from the frontal geostrophic shear (Figure 9a). However, the
388   GSP profile in the coarse-resolution case KPP550 is relatively weak as it results only from the
389   KPP vertical viscosity damping of the sheared front (blue line in Figure 9a). In contrast, the GSP
390   in the SML in the high-resolution case KPP55 (red line in Figure 9a) is enhanced by about 2 ~ 3
391   times over KPP550. This GSP enhancement is attributed to the resolved SI in the high-resolution
392   case that grows by extracting frontal kinetic energy and weakening the frontal geostrophic shear.
393   The SI scheme is designed to mimic this behavior, and when activated in the coarse-resolution
394   simulation SI550, the calculated GSP profile (green line in Figure 9a) is obviously improved and
395   closer to the high-resolution case.

396   Under the SI-induced vertical buoyancy flux, the BF is also expected to be enhanced in
397   the SML (Figure 9b). Figure 9b indeed shows the BF is negative and weak below the SML,
398   consistently in the three cases. The weak negative BF is the signature of entrainment through
399   vertical mixing (Grant & Belcher, 2009; Li & Fox-Kemper, 2017, 2020). In the SML, the BF
400   becomes positive indicating restratification of the SML via both surface forcing and entrained
401   fluid. Two processes may contribute to this restratification. One is the convection process near
402   the surface. The surface cooling leads to surface buoyancy loss and weaker stratification in the
403   SML, carried out by the vertical convection and upward buoyancy flux (dense water moving
404   downward). The other process is SI. To restore PV to a neutral state (i.e., PV=0) and reach
405   marginal SI stability, the overturning cells associated with SI tend to flatten the slanted
406   isopycnals at fronts, leading to restratification (Bachman & Taylor, 2014; B17). In KPP550, the
407   positive BF can only be caused by surface convection. However, as the resolution increases, the
408   BF is enhanced especially at the lower SML in KPP55 with a notable increase of more than 60%
409   near 25 m depth—indicative of the resolved SI restratification. The SI scheme is designed to
410   mimic the enhanced BF and the SI550 simulation indeed becomes closer to the high-resolution
411   BF result of KPP55. Compared with the high-resolution result, a similar parameterized increase
412   of about 50% in the SI550 at about 25 m depth is observed. Given that the buoyancy flux forcing
413   inducing convection is consistent between the three cases, the enhancement at the lower SML in
414   the SI550 and KPP55 is cleanly attributable to SI restratification.

415   Unlike the GSP and BF, the BP associated with MLI is modestly weakened during
416   simulation days 8 through 12 if the SI impacts are resolved or parameterized (Figure 9c).
417   Generally, the BP is zero below the SML but positive in the SML, implying available potential
418   energy release (e.g., Boccaletti et al., 2007; Fox-Kemper et al., 2008). This positive BP also
419   indicates SML restratification by MLI, which should be the dominant or a significant factor for
420   the SML shallowing in the coarse-resolution case KPP550 (Figure 6d and Figure 8d), as the SI
421   impacts are not included in that simulation. In this case, the SI plus convective restratification
422   BF exceeds the MLI restratification BP, but as the different effects scale very differently with
423   frontal strength and surface forcing (Fox-Kemper et al., 2008; B17), this is not expected to be a
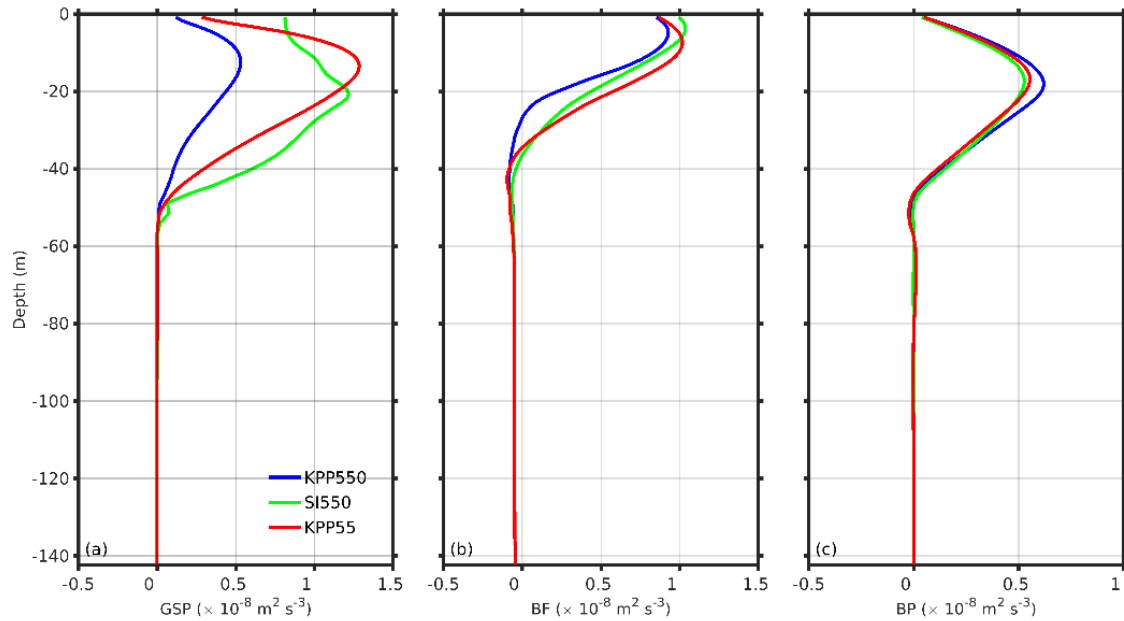424   general result.

425
426   Figure 9 Vertical profiles of (a) geostrophic shear production, GSP ($m^2\ s^{-3}$), (b) vertical
427   buoyancy flux, BF ($m^2\ s^{-3}$), and buoyancy production, BP ($m^2\ s^{-3}$) averaged over a 30km region
428   enclosing NFront during cooling periods of simulation days 8 through 12.

429

430   The GSP, BF and BP capture the different kinetic and potential energy production due to
431   SI among the three simulations. Rather than averaging over windows, the total time evolution of
432   the kinetic energy and potential energy densities averaged over NFront are analyzed (Figure 10)
433   which reveal directly the integrated effects of these distinct energy budgets among the models. In
434   addition to diurnal and inertial oscillation variability, the kinetic energy of the along-front
435   currents (i.e., in y-direction average) shows differences between three cases: the magnitudes in
436   both SI550 and KPP55 are generally weaker than that in KPP550 after 10 days (Figure 10a),
437   although the differences are modest in comparison to the oscillations present in all three runs.
438   The enhanced GSP due to SI contributes to the differences. If the ageostrophic Ekman and
439   inertial currents are removed, the kinetic energy of the geostrophic currents (diagnosed from the
440   along-front averaged density fields) dominates the total along-front kinetic energy (Figure 10b).
441   The relatively weaker kinetic energy is still observed in SI550 and KPP55.

442   One aspect of the energy cycle obscuring the SI effect is that the submesoscale kinetic
443   energy related to MLI is also modulated by SI (Figure 10c), as suggested by the BP in Figure 9d.
444   As MLI begin to grow (after 8 days), the submesoscale kinetic energy increase is slowed down
445   in both SI550 and KPP55, compared with the result in KPP550 (Figure 10c). This evolution is
446   consistent with the calculated BP profiles in Figure 9d, since the BP that fuels MLI is weakened
447   when SI is resolved or parameterized, suppressing MLI. However, this situation is reversed after
448   about 12 days. Then submesoscale kinetic energy becomes stronger in SI550 and KPP55, as
449   more potential energy is converted into MLI. Apparently, BP is strengthened after 12 days (not
450   shown). The potential energy over NFront decreases consistently during the simulation, and
451   slightly lower energy content can be observed in SI550 and KPP55, especially after 15 days
452   (Figure 10d), a difficult to anticipate result of both the enhanced mixing and enhanced

453   restratification in these runs. Note that even while the energetic consequences of SI are modest in
454   comparison to other changes in these simulations, the effects on stratification and PV are not (see
455   next section).

456   The energetic analysis here indicates that SI can not only decrease the frontal geostrophic
457   shear, but also modulate the growth of MLI. The MLI kinetic energy evolution is firstly
458   suppressed at the beginning and then enhanced due to the impacts of SI. The primary goal of this
459   work is focused on the implementation and effects of the SI parameterization in the CROCO, and
460   further analysis about the interactions between SI and MLI are not conducted here. Underlying
461   mechanisms for the interactions need be clarified in the future, although it is perhaps telling—or
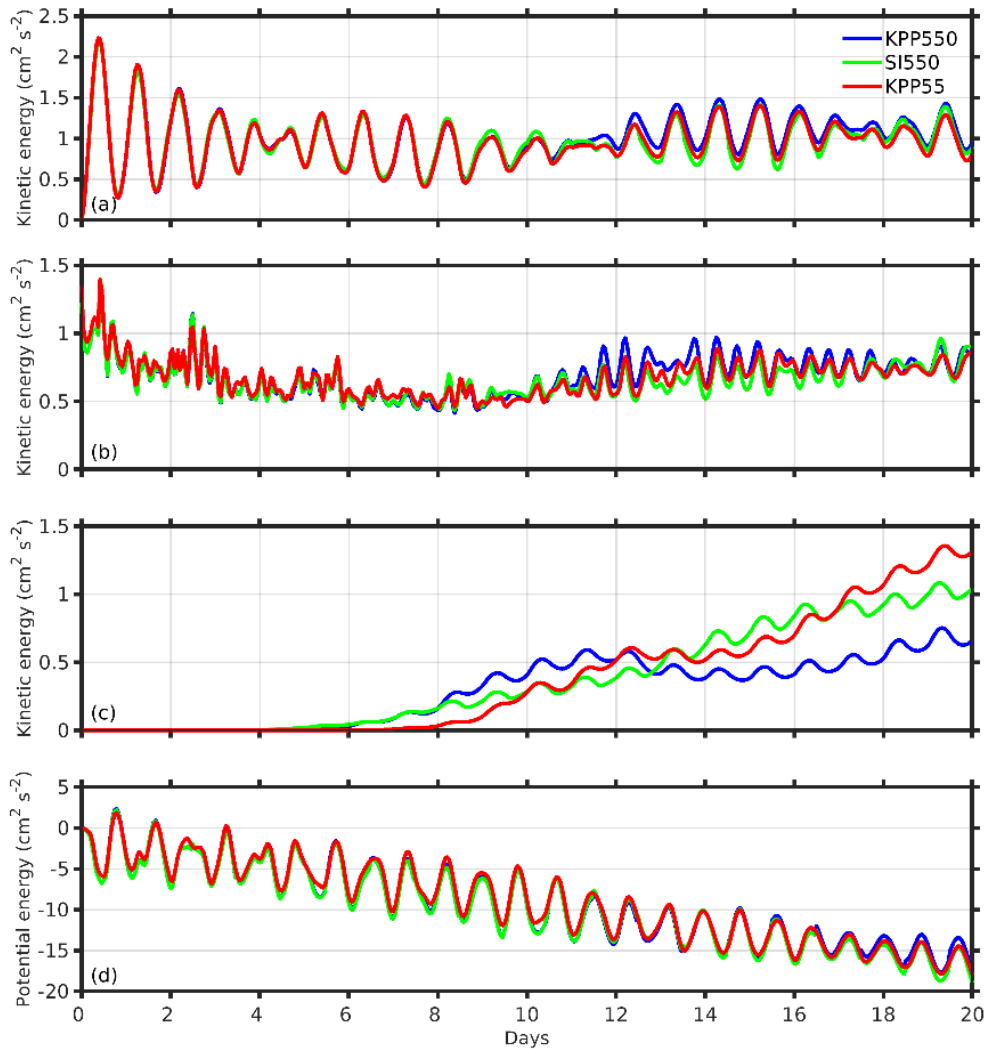462   coincidental—that the effect is common to both the resolved and parameterized SI.

463
464   Figure 10 Time evolution of the (a) along-front kinetic energy density ($cm^2\ s^{-2}$), (b) along-front
465   geostrophic kinetic energy density ($cm^2\ s^{-2}$), (c) MLI kinetic energy density ($cm^2\ s^{-2}$) and (d)
466   potential energy density ($cm^2\ s^{-2}$) averaged on over NFront.
467

468   3.3 Mixed layer thickness and potential vorticity

469   The transverse sections of temperature and PV in Figure 6 and Figure 8 show the SML
470 shoaling as SI is resolved or parameterized. Quantitative analysis of the mixed layer thickness
471 changes is conducted in this section. Here, the mixed layer thickness is defined as the depth at
472 which the surface potential density increases by a value of 0.03 kg m^{-3} (following de Boyer
473 Montégut et al. (2004)). The mixed layer depth averaged over NFront has a shoaling trend over
474 the simulation time (Figure 11a). The mixed layer thickness tends to vary in conjuction with MLI
475 energy. Initially, the mixed layer thicknesses in the three cases covary in time. As MLI begins to
476 grow after 8 days, the mixed layer thicknesses begin to differ. SI550 and KPP55 have slightly
477 deeper mixed layers at this stage compared with the KPP550, but they grow shallower as time
478 evolves. There is quantitative agreement in differences of the mixed layer thicknesses between
479 SI550 and KPP550 (green line in Figure 11b) and KPP55 and KPP550 (red line in Figure 11b)
480 over time. The difference is positive and less than 1 m between simulation days 8 and 10, but
481 afterward becomes negative between 1 ~ 2 m. Compared with the overall mixed layer thickness,
482 the SI effect accounts for a small fraction in these simulations. However, how much SI
483 contributes to the mixed layer restratification depends on the SI activity and strength, so a
484 realistic simulation is needed for quantitative assessment.

485   The mixed layer depth covaries with MLI kinetic energy, but this correlation may not be
486 causal. The SML restratification is induced by SI as well in two ways: the upward buoyancy flux
487 associated with MLI is modulated by SI, which shoals the SML, and SI tends to flatten
488 isopycnals to reduce negative PV, leading to SML restratification. It is hard to distinguish these
489 two SI and the perturbed MLI contributions here, but one can attribute the total changes to SI as
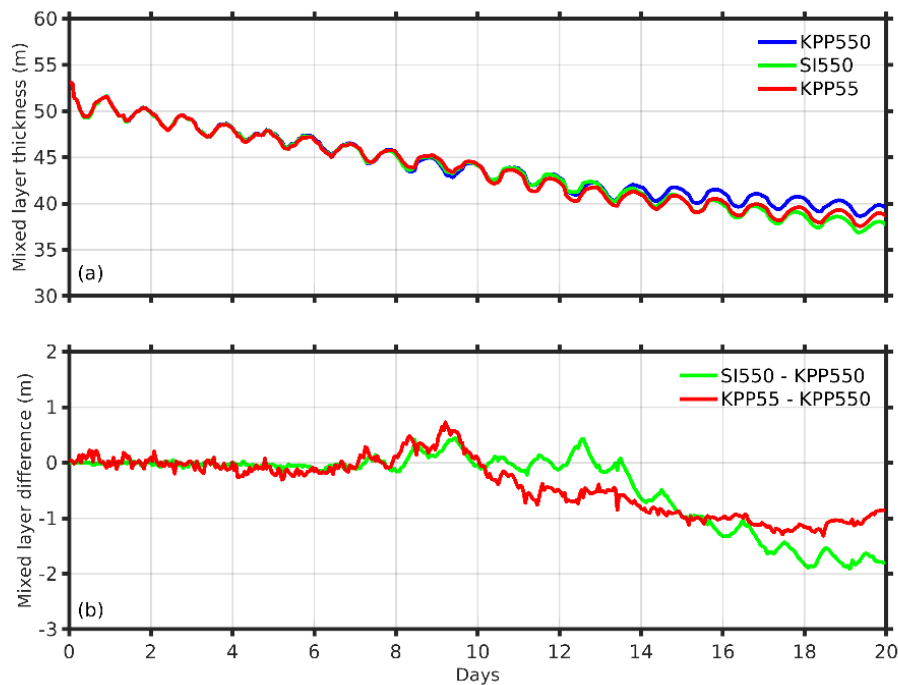490 parameterized or resolved.

492 Figure 11 Time evolution of (a) mixed layer thickness (m) and (b) differences (m) averaged over
493 NFront. The mixed layer thickness is determined with a threshold potential density value of 0.03
494 kg m^{-3} (de Boyer Montégut et al., 2004).

495
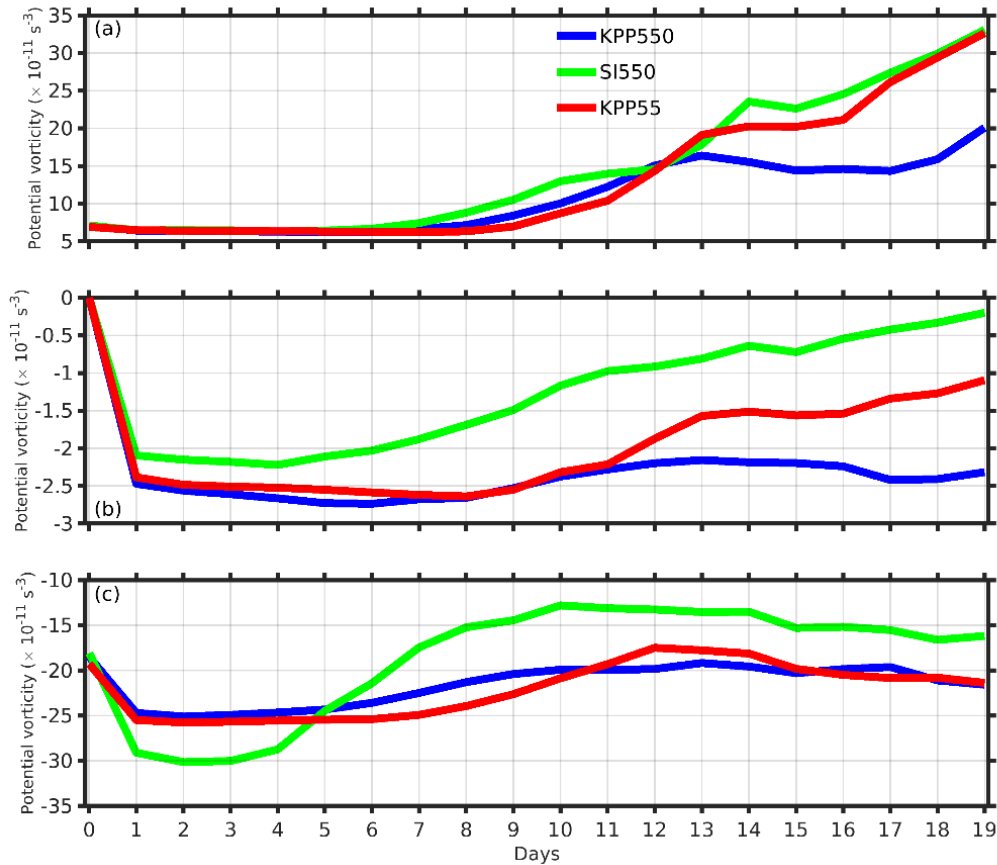
496　　　　A direct impact from SI is the ability to reduce negative PV and restore PV to a neutral
497　state. Different percentiles of PV in the upper 30 over NFront demonstrate this impact from SI
498　(Figure 12). Due to the horizontal buoyancy gradients of the front, the median PV is negative in
499　the three cases (Figure 12b). The median PV in both SI550 and KPP55 is closer to zero (neutral
500　state) as expected, compared with KPP550, as SI is expected to bring up stratified thermocline
501　waters to oppose surface forcing and approach marginal stability for SI—zero PV. Meanwhile,
502　the reduction of negative PV also shifts the 10th and 90th percentiles, an indicator of the complex
503　spatial variety of the SI-MLI combination illustrated in Figures 5 and 8. The 10th percentile of
504　PV in SI550 is shifted to a smaller negative value in contrast to KPP550 and KPP55 (Figure
505　12c). PV is scale-dependent, and the magnitude of surface forcing will become larger as grid
506　spacings become finer (Bodner & Fox-Kemper, 2020). But the 10th PV in KPP55 is comparable
507　with the value in the KPP550 here. For the 90th percentile of PV, it is positive and moves to
508　larger values under the SI impact (Figure 12a), consistently among the resolved- and
509　parameterized-SI cases.

510
511　Figure 12 Time evolution of the (a) 90th percentile, (b) median and (c) 10th percentile values of
512　PV (s^{-3}) in the upper 30 m over NFront.

513

514　　　　The probability density functions (PDF) of PV in the upper 30 m (within the SML) at the
515　last day in the three cases are calculated and shown in Figure 13. The PDF of PV is clearly

516   modulated by SI. A consistent elevated tail on the positive PV value side of the PDF occurs in
517   both SI550 and KPP55 (Figure 13a). For negative PV values, the PDF tail in SI550 is depressed,
518   while in contrast KPP55 is depressed only for weaker values (roughly PV≥−0.5×10^{-9} s^{-3}) and
519   elevated for more negative PV. Large negative PV probability in KPP55 is significantly higher
520   than either KPP550 or SI550, which may not be an effect of SI but rather an attribute of PV
521   injection due to the finer grid spacings. The PDFs in all cases have positive skewnesses due to
522   centrifugal instability (e.g., Capet et al., 2008b). Overall, SI changes the asymmetry of the PDF
523   by elevating positive PV and decreasing negative PV (although surface forcing counters this
524   effect). The calculated skewness of the PDF in KPP550 is 0.11, and increased to 0.16 and 0.15 in
525   SI550 and KPP55, respectively. The PV reduction by SI is further highlighted if we integrate the
526   PDFs over the negative PV range (Figure 13b). The probability of negative PV in KPP55 is 0.61,
527   but decreases to 0.51 in SI550 and 0.54 in KPP55.
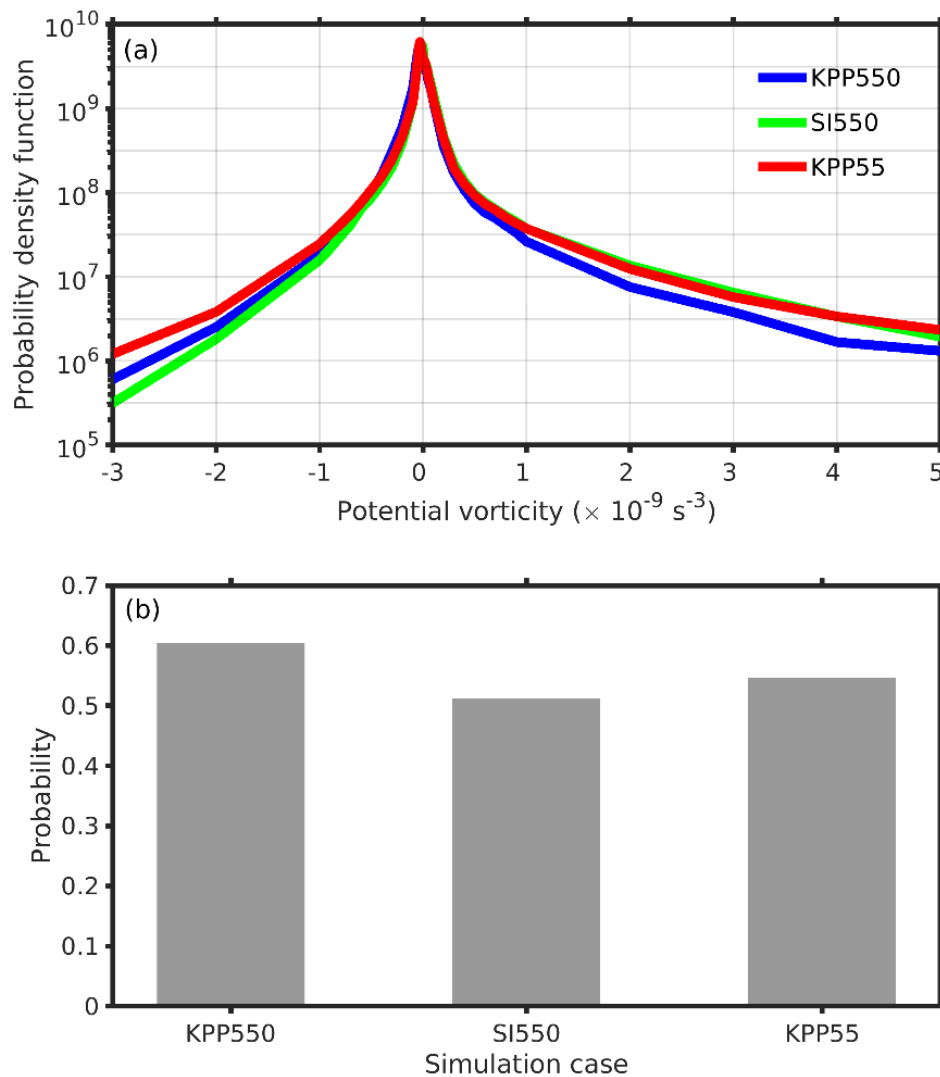

528
529   Figure 13 (a) Probability density functions of PV and (b) the probabilities of negative PV in the
530   upper 30 m over NFront at the last day of the simulation in different cases.
531

532   3.4 Tracer redistribution

533   The impacts on tracer redistribution by SI diffusivity are assessed by releasing two types
534 of tracers in these three cases. The tracer fields are homogeneous in horizontal but vary in
535 vertical following a hyperbolic tangent function. The concentration of the first type, C0 has a
536 decreasing trend with depth, namely,

$$C0 = \frac{1}{2}\left(1 - \tanh\left(\frac{z+30}{5}\right)\right). \tag{21}$$

538 C0 represents tracers that are scarce near the surface but abundant in deep (e.g., nutrients). In
539 contrast, the concentration of the second type, C1 represents tracers that are abundant near the
540 surface (e.g., CO_2),

$$C1 = \frac{1}{2}\left(1 + \tanh\left(\frac{z+30}{5}\right)\right). \tag{22}$$

542 No surface exchanges are applied for these tracers. Both tracers are released at 12 days and
543 simulated for 5 days.

544   The tracer concentrations averaged over NFront are shown in Figure 14. The tracer
545 gradients with initial depths around 30 m deepen toward the pycnocline as time evolves in all
546 three cases. The concentration of C0 at the surface increases with time due to the vertical tracer
547 flux (Figure 14a, c, e), while that of C1 at the surface decreases with time (Figure 14b, d, f).
548 Overall, the evolution of the tracers shows similar patterns. The final profiles of the tracers
549 averaged over NFront indicates the differences between the three cases (Figure 15). Compared
550 with KPP550, SI550 reproduces the tracer profiles closer to the high-resolution case KPP55. The
551 differences reach as much as 0.07 between SI550 and KPP550, and 0.05 between KPP55 and
552 KPP550. The most notable differences mainly occur between 20 m and 60 m, emphasizing the
553 importance of SI on exchanges between the SML and ocean interior. It should be noted that the
554 impacts of SI on the tracer redistribution highly depends on the averaging region, initial vertical
555 tracer profiles and SI activity. Nevertheless, the results here highlight that SI and the SI scheme
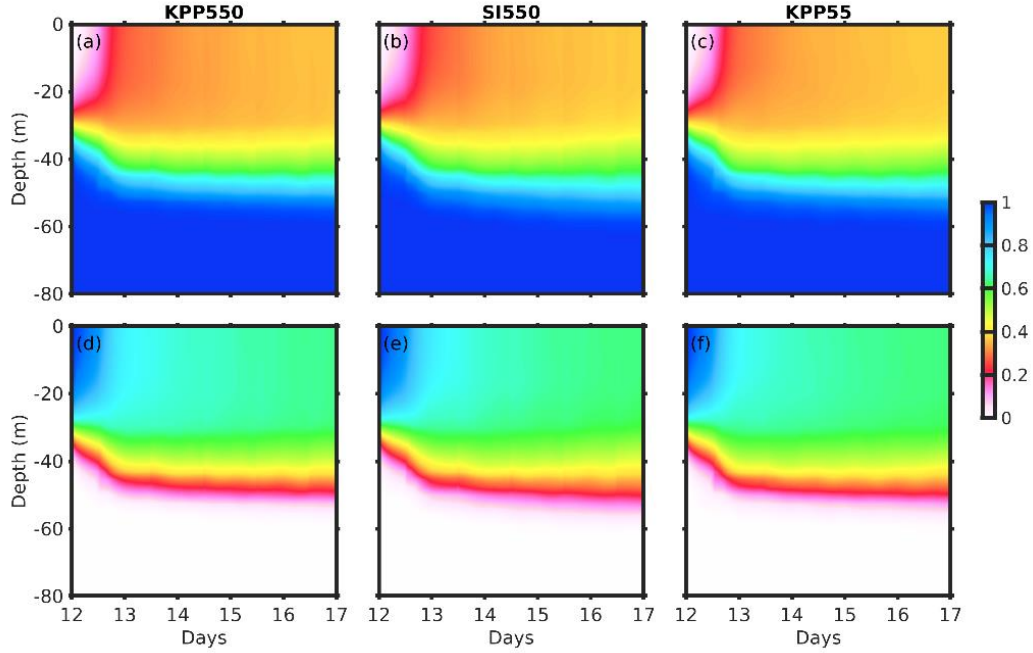556 affect tracer redistribution, particularly near the ML base.

557
558   Figure 14 Time evolution of the tracer concentration profiles averaged over NFront in (a, d)
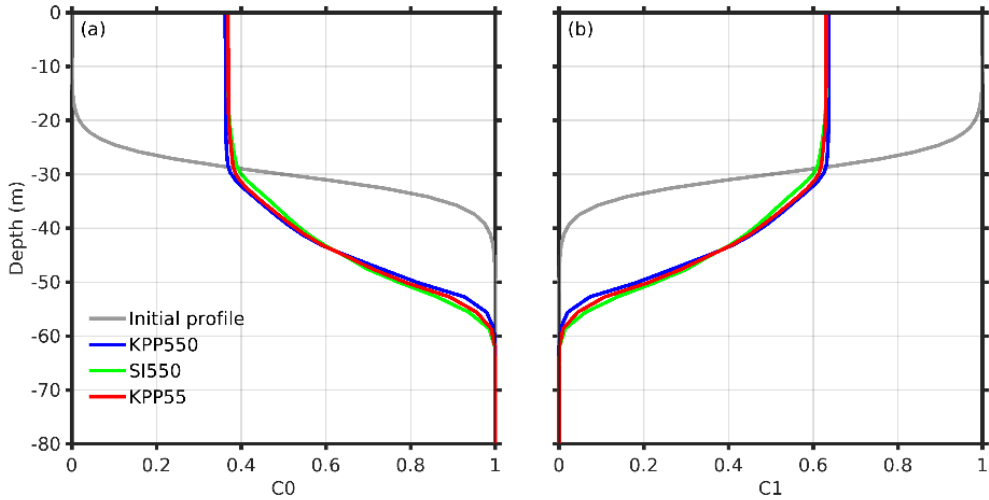559   KPP550, (b, e) SI550 and (c, f) KPP55.

560
561   Figure 15 Tracer profiles of (a) C0 and (b) C1 averaged over NFront at the end of 16 days in
562   different cases. The gray lines denote the initial profiles released at 12 days.

563

4 Discussion and Conclusions

565   Based on the analysis above, the SI scheme parameterizes the impacts of SI in a SI-
566   unresolved model in many regards. Despite of the good consistency between the coarse-
567   resolution case SI550 and the high-resolution case KPP55, several limitations remain. First of all,
568   the SI scheme applied here is engaged only when both B_0 and *EFB* are positive—i.e., *forced* SI.
569   However, the cross-front velocity perturbations in Figure 4 indicate that SI occurs at the front

570   even when B_0 is negative. As the control case to directly resolve SI, the high-resolution case is
571   also limited in capturing the full SI effects.

572   4.1 SI resolving and nonhydrostatic effect

573   Based on the estimation in Section 2, the initial temperature field allows that the fastest
574   SI growing modes have spatial wavelengths between 0.5 ~ 1.5 km. It can be inferred that the SI
575   scales vary as the front evolves. Based on the output variables from KPP55, the SI wavelengths
576   are estimated based on Equation (2). Here, U and Ri_b are calculated based on the model outputs.
577   Theoretically Ri_b is between $0.25 \leqslant Ri_b \leqslant 0.95$ for SI dominance, so here Ri_b is an average in the
578   SI layer and arbitrarily assigned to be $Ri_b=0.25$ when $Ri_b<0.25$ and $Ri_b=0.95$ when $Ri_b>0.95$.
579   Given that the upper limit wavelength of dynamic processes for a model to resolve is two times
580   of the grid spacings (a requirement from the Nyquist sampling rate), SI that resolved by KPP55
581   should have wavelengths larger than 110 m. Based on this threshold value, the percentage of the
582   resolved SI in KPP55 is estimated (Figure 16a). Here, the resolved-SI percentage is defined as
583   the percentage of grid points with SI wavelengths larger than 110 m over the total grid points
584   with $h < 0.95H$. According to the estimation, the resolved-SI percentage reaches 70% at the
585   beginning and decrease to about 40% at the end of the simulation. Bachman & Taylor (2014)
586   show that the SI growth curve typically extends about a factor of 2−3 smaller than the peak
587   growth rate, and they argue that these smaller scales are needed for quantitative although not
588   qualitative accuracy.

589   The small SI spatial scales may also potentially invalidate the hydrostatic approximation
590   used here. To measure this potential nonhydrostatic impact, the hydrostatic parameter of the
591   resolved SI is calculated as (Marshall et al., 1997; Bachman & Taylor, 2014),

592
$$\eta = \frac{\delta^2}{Ri_b},$$
(23)

593   where $\delta = H/L_{SI}$ is the aspect ratio, H is the SI layer determined by Equation (3) that can be taken
594   as the vertical scale of SI, and L_{SI} is the SI wavelength determined by Equation (2). The
595   hydrostatic approximation is appropriate and the nonhydrostatic impact is negligible when $\eta \ll 1$.

596   The hydrostatic parameter at different percentiles and days are shown in Figure 16b. It
597   can be observed that the resolved SI has hydrostatic parameter values up to 0.5, indicating that
598   the nonhydrostatic impact may become important for the smallest SI. However, 85% ~ 95% of
599   the SI as resolved during the simulation period has hydrostatic parameter values less than 0.1
600   (black line in Figure 16b). The nonhydrostatic effect is believed to be limited for this case here.
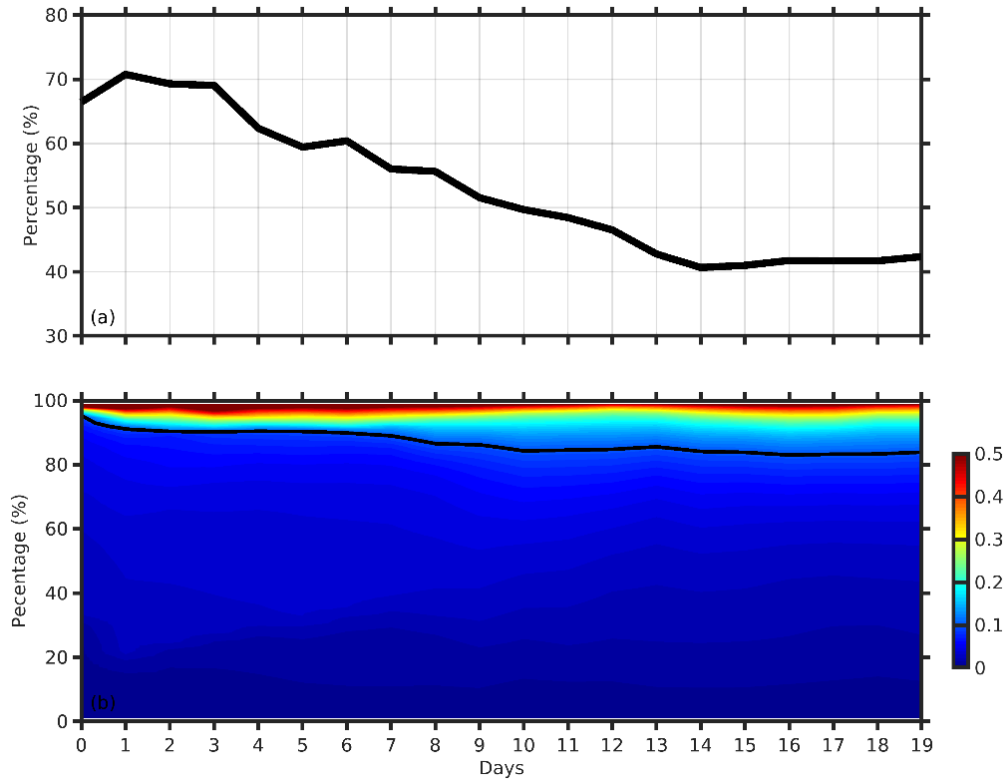
Figure 16 (a) The estimated percentage (%) of the resolved SI and (b) the hydrostatic parameter η distribution in KPP55 during the simulation period. The black line in (b) shows the isoline of η=0.1.

4.2 Prandtl number relation

According to B17, the Prandtl number, *Pr* is an important parameter to link the SI diffusivity and viscosity, which can be evaluated as,

$$Pr = \frac{v_{SI}}{\kappa_{SI}} = \frac{-v_{SI}w_{SI}\left(\frac{\partial v_g}{\partial z}\right)^{-1}}{-w_{SI}b_{SI}\left(\frac{\partial b_b}{\partial z}\right)^{-1}}. \tag{24}$$

In the SI scheme, the relation of *Pr* used follows the expression suggested by Anderson (2009),

$$Pr = \frac{1+(10Ri_b)^{0.8}}{2}. \tag{25}$$

Based on the KPP55 results, the calculated *Pr* in the SI-dominated layer (the same depth range with B17, $-1.2h{>}z{>}{-}H$) can be compared to this relation. Similar to the results calculated from LES results in B17, the calculated *Pr* values are scattered in $0{\leqslant}Ri_b{\leqslant}1$. Following the work by B17, the median, 20th and 80th percentile values in each Ri_b bin (a bin size of 0.1) are calculated and shown (solid line with error bars in Figure 17). Compared with the suggested *Pr* relation, the median *Pr* calculated from KPP55 almost follows the empirical relation at low Ri_b, but generally becomes smaller. The partially SI resolving and hydrostatic approximation may exert impacts on the *Pr* estimate. However, doubts may also exist in the robustness of the empirical relation to describe the relation between SI viscosity and diffusivity. The *Pr* relation is beyond the scope of

620   this work, and likely requires a nonhydrostatic model to examine, but further work is definitely
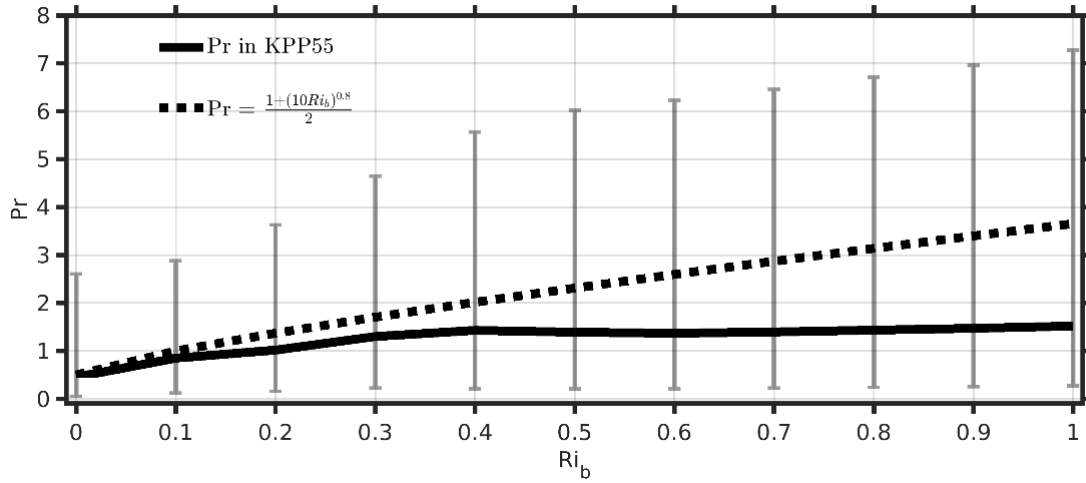621   needed to improve the SI scheme.

622

623   Figure 17 The median *Pr* versus Ri_b in KPP55 (solid line). The error bars denote the 20th
624   and 80th percentile *Pr* values. The dash line denotes the empirical relation between *Pr* and Ri_b in
625   Equation (25).

626

627   4.3 Conclusions

628   The SI scheme proposed by B17 is applied alongside the KPP scheme in the CROCO in
629   this work, and the analysis based on the idealized model simulations indicates positive
630   improvements of the simulation results by the SI scheme.

631   The GSP is the dominant energy source for SI, and the calculated GSP is remarkably
632   enhanced in these simulations as the model resolution becomes fine enough to resolve SI (KPP55
633   vs. KPP550). The results from SI550 indicates that the SI scheme improves the GSP magnitude
634   more closely matching the high-resolution case KPP55. In addition to the GSP, the vertical heat
635   fluxes BF (turbulent) and BP (submesoscale) are also modulated by SI. These impacts are also
636   captured by the SI scheme.

637   Overall, the SML by SI impacts, which is both a direct SI impact and an indirect SI
638   impact through modulating MLI and BP. A primary role of SI is to reduce negative PV. Here SI
639   shifts the median PV closer to a neutral state of PV=0. In order for SI to reduce negative PV, the
640   positive PV becomes more likely in the SI-resolved and SI-parameterized runs than the SI-
641   neglected KPP550 run. Moreover, passive tracers indicate potential contributions of SI on
642   exchanges between the SML and ocean interior.

643   These simulations indicate the significant effects of the SI scheme in a coarse-resolution
644   model, but the quantitative values in this work are based on idealized model simulations with an
645   idealized front. To measure SI contributions in the real oceans, a more realistic model with and
646   without the SI scheme included must be compared.

647

References

660 Anderson, P. S. (2009). Measurement of Prandtl number as a function of Richardson number
661 avoiding self-correlation. *Boundary-layer meteorology*, *131*(3), 345-362. doi:10.1007/s10546-
662 009-9376-4

663 Bachman, S. D., & Taylor, J. R. (2014). Modelling of partially-resolved oceanic symmetric
664 instability. *Ocean Modelling*, *82*, 15-27. doi:10.1016/j.ocemod.2014.07.006

665 Bachman, S. D., Fox-Kemper, B., Taylor, J. R., & Thomas, L. N. (2017). Parameterization of
666 frontal symmetric instabilities. I: Theory for resolved fronts. *Ocean Modelling*, *109*, 72-95.
667 doi:10.1016/j.ocemod.2016.12.003

668 Boccaletti, G., Ferrari, R., & Fox-Kemper, B. (2007). Mixed layer instabilities and
669 restratification. *Journal of Physical Oceanography*, *37*(9), 2228-2250. doi:10.1175/JPO3101.1

670 Bodner, A., & Fox-Kemper. B. (2020) A breakdown in potential vorticity estimation delineates
671 the submesoscale-to-turbulence boundary in large eddy simulations. *Journal of Advances in
672 Modeling Earth Systems*, *12*, e2020MS002049. doi:10.1029/2020MS002049

673 Buckingham, C. E., Lucas, N., Belcher, S., Rippeth, T., Grant, A., Le Sommer, J., . . . Garabato,
674 A. C. N. (2019). The contribution of surface and submesoscale processes to turbulence in the
675 open ocean surface boundary layer. *Journal of Advances in Modeling Earth Systems*, 11(12),
676 4066-4094. doi:10.1029/2019MS001801

677 Buckingham, C. E., Naveira Garabato, A. C., Thompson, A. F., Brannigan, L., Lazar, A.,
678 Marshall, D. P., . . . Belcher, S. E. (2016). Seasonality of submesoscale flows in the ocean
679 surface boundary layer. *Geophysical Research Letters*, *43*(5), 2118-2126.
680 doi:10.1002/2016GL068009

681 Callies, J., Ferrari, R., Klymak, J. M., & Gula, J. (2015). Seasonality in submesoscale turbulence.
682 *Nature Communications*, *6*, 6862. doi:10.1038/ncomms7862

683 Capet, X., McWilliams, J. C., Molemaker, M. J., & Shchepetkin, A. (2008a). Mesoscale to
684 submesoscale transition in the California Current System. Part III: Energy balance and flux.
685 *Journal of Physical Oceanography*, *38*(10), 2256-2269. doi:10.1175/2008JPO3810.1

686 Capet, X., McWilliams, J. C., Molemaker, M. J., & Shchepetkin, A. F. (2008b). Mesoscale to
687 submesoscale transition in the California Current System. Part I: Flow structure, eddy flux, and

688   observational tests. *Journal of Physical Oceanography*, *38*(1), 29-43. doi:
689   10.1175/2007JPO3671.1

690   D'Asaro, E., Lee, C., Rainville, L., Harcourt, R., & Thomas, L. (2011). Enhanced turbulence and
691   energy dissipation at ocean fronts. *Science*, *332*(6027), 318-322. doi:10.1126/science.1201515

692   de Boyer Montégut, C., Madec, G., Fischer, A. S., Lazar, A., & Iudicone, D. (2004). Mixed layer
693   depth over the global ocean: An examination of profile data and a profile-based climatology.
694   *Journal of Geophysical Research: Oceans*, *109*(C12). doi:10.1029/2004JC002378

695   de Marez, C., Carton, X., Corréard, S., L'Hégaret, P., & Morvan, M. (2020). Observations of a
696   deep submesoscale cyclonic vortex in the Arabian Sea. *Geophysical Research Letters*, *47*(13),
697   e2020GL087881. doi:10.1029/2020GL087881

698   Dong, J., Fox-Kemper, B., Zhang, H., & Dong, C. (2020a). The seasonality of submesoscale
699   energy production, content, and cascade. *Geophysical Research Letters*, e2020GL087388.
700   doi:10.1029/2020GL087388

701   Dong, J., Fox-Kemper, B., Zhang, H., & Dong, C. (2020b). The scale and activity of symmetric
702   instability globally. *Journal of Physical Oceanography*, under review.
703   http://www.geo.brown.edu/research/Fox-Kemper/pubs/pdfs/DongFox-Kemper20b.pdf

704   Fox-Kemper, B., Danabasoglu, G., Ferrari, R., Griffies, S. M., Hallberg, R. W., Holland, M. M.,
705   . . . Samuels, B. L. (2011). Parameterization of mixed layer eddies. III: Implementation and
706   impact in global ocean climate simulations. *Ocean Modelling*, *39*(1-2), 61-78.
707   doi:10.1016/j.ocemod.2010.09.002

708   Fox-Kemper, B., Ferrari, R., & Hallberg, R. (2008). Parameterization of mixed layer eddies. Part
709   I: Theory and diagnosis. *Journal of Physical Oceanography*, *38*(6), 1145-1165.
710   doi:10.1175/2007JPO3792.1

711   Grant, A.L. and Belcher, S.E., 2009. Characteristics of Langmuir turbulence in the ocean mixed
712   layer. *Journal of Physical Oceanography*, *39*(8), pp.1871-1887. doi:10.1175/2009JPO4119.1

713   Gula, J., Molemaker, M. J., & McWilliams, J. C. (2016). Topographic generation of
714   submesoscale centrifugal instability and energy dissipation. *Nature Communications*, *7*, 12811.
715   doi:10.1038/ncomms12811

716   Haine, T. W., & Marshall, J. (1998). Gravitational, symmetric, and baroclinic instability of the
717   ocean mixed layer. *Journal of Physical Oceanography*, *28*(4), 634-658. doi:10.1175/1520-
718   0485(1998)028<0634:GSABIO>2.0.CO;2

719   Hamlington, P. E., Van Roekel, L. P., Fox-Kemper, B., Julien, K., & Chini, G. P. (2014).
720   Langmuir–submesoscale interactions: Descriptive analysis of multiscale frontal spindown
721   simulations. *Journal of Physical Oceanography*, *44*(9), 2249-2272. doi:10.1175/JPO-D-13-
722   0139.1

723   Haney, S., Fox-Kemper, B., Julien, K., & Webb, A. (2015). Symmetric and geostrophic
724   instabilities in the wave-forced ocean mixed layer. *Journal of Physical Oceanography*, *45*(12),
725   3033-3056. doi:10.1175/JPO-D-15-0044.1

726   Hedström, K., (2009). Technical Manual for a Coupled Sea-Ice/Ocean Circulation Model
727   (Version 3). U.S. Department of the Interior Minerals Management Service Anchorage, Alaska
728   (2009) Contract No. M07PC13368.

729   Hoskins, B. (1974). The role of potential vorticity in symmetric stability and instability.
730   *Quarterly Journal of the Royal Meteorological Society*, *100*(425), 480-482.
731   doi:10.1002/qj.49710042520

732   Jullien, S., Caillaud, M., Benshila, R., Bordois, L., Cambon, G., Dumas, F., Le Gentil, S.,
733   Lemarié, F., Marchesiello, P., & Theetten, S. (2019). Technical and numerical doc.
734   https://www.croco-ocean.org/documentation/

735   Large, W. G., McWilliams, J. C., & Doney, S. C. (1994). Oceanic vertical mixing: A review and
736   a model with a nonlocal boundary layer parameterization. *Reviews of Geophysics*, *32*(4), 363-
737   403. doi:10.1029/94RG01872

738   Lévy, M., Ferrari, R., Franks, P. J., Martin, A. P., & Rivière, P. (2012). Bringing physics to life
739   at the submesoscale. *Geophysical Research Letters*, *39*(14). doi:10.1029/2012GL052756.
740   doi:10.1029/2012GL052756

741   Li, Q., Webb, A., Fox-Kemper, B., Craig, A., Danabasoglu, G., Large, W. G., & Vertenstein, M.
742   (2016). Langmuir mixing effects on global climate: WAVEWATCH III in CESM. *Ocean
743   Modelling*, *103*, 145-160. doi:10.1016/j.ocemod.2015.07.020

744   Li, Q. and Fox-Kemper, B., 2017. Assessing the effects of Langmuir turbulence on the
745   entrainment buoyancy flux in the ocean surface boundary layer. *Journal of Physical
746   Oceanography*, *47*(12), pp.2863-2886. doi:10.1175/JPO-D-17-0085.1

747   Li, Q. and Fox-Kemper, B., 2020. Anisotropy of Langmuir turbulence and the Langmuir-
748   enhanced mixed layer entrainment. *Physical Review Fluids*, *5*(1), p.013803.
749   doi:10.1103/PhysRevFluids.5.013803

750   Marshall, J., Hill, C., Perelman, L., & Adcroft, A. (1997). Hydrostatic, quasi-hydrostatic, and
751   nonhydrostatic ocean modeling. *Journal of Geophysical Research: Oceans*, *102*(C3), 5733-5752.
752   doi:10.1029/96JC02776

753   McWilliams, J. C. (2016). Submesoscale currents in the ocean. *Proceedings of the Royal Society
754   A*, *472*(2189), 20160117. doi:10.1098/rspa.2016.0117

755   Molemaker, M. J., McWilliams, J. C., & Dewar, W. K. (2015). Submesoscale instability and
756   generation of mesoscale anticyclones near a separation of the California Undercurrent. *Journal
757   of Physical Oceanography*, *45*(3), 613-629. doi:10.1175/JPO-D-13-0225.1

758   Noh, Y., Ok, H., Lee, E., Toyoda, T., & Hirose, N. (2016). Parameterization of Langmuir
759   circulation in the ocean mixed layer model using LES and its application to the OGCM. *Journal
760   of Physical Oceanography*, *46*(1), 57-78. doi:10.1175/JPO-D-14-0137.1

761   Qiao, F., Yuan, Y., Deng, J., Dai, D., & Song, Z. (2016). Wave–turbulence interaction-induced
762   vertical mixing and its effects in ocean and climate models. *Philosophical Transactions of the
763   Royal Society A: Mathematical, Physical and Engineering Sciences*, *374*(2065), 20150201.
764   doi:10.1098/rsta.2015.0201

765   Redi, M. H. (1982). Oceanic isopycnal mixing by coordinate rotation. *Journal of Physical
766   Oceanography*, *12*(10), 1154-1158. doi:10.1175/1520-
767   0485(1982)012<1154:OIMBCR>2.0.CO;2

768 Siegelman, L., Klein, P., Rivière, P., Thompson, A. F., Torres, H. S., Flexas, M., & Menemenlis,
769 D. (2019). Enhanced upward heat transport at deep submesoscale ocean fronts. *Nature*
770 *Geoscience*, 1-6. doi:10.1038/s41561-019-0489-1

771 Smith, K. M., Hamlington, P. E., & Fox-Kemper, B. (2016). Effects of submesoscale turbulence
772 on ocean tracers. *Journal of Geophysical Research: Oceans*, *121*(1), 908-933.
773 doi:10.1002/2015JC011089

774 Stone, P. H. (1966). On non-geostrophic baroclinic stability. *Journal of the atmospheric*
775 *sciences*, *23*(4), 390-400. doi:10.1175/1520-0469(1966)023<0390:ONGBS>2.0.CO;2

776 Su, Z., Wang, J., Klein, P., Thompson, A. F., & Menemenlis, D. (2018). Ocean submesoscales as
777 a key component of the global heat budget. *Nature Communications*, *9*(1), 775.
778 doi:10.1038/s41467-018-02983-w

779 Taylor, J. R., & Ferrari, R. (2010). Buoyancy and wind-driven convection at mixed layer density
780 fronts. *Journal of Physical Oceanography*, *40*(6), 1222-1242. doi:10.1175/2010JPO4365.1

781 Thomas, L. N. (2005). Destruction of potential vorticity by winds. *Journal of Physical*
782 *Oceanography*, *35*(12), 2457-2466. doi:10.1175/JPO2830.1

783 Thomas, L. N., Tandon, A., & Mahadevan, A. (2008). Submesoscale processes and dynamics.
784 *Ocean modeling in an Eddying Regime*, 17-38. doi:10.1029/177GM04. doi:10.1029/177GM04

785 Thomas, L. N., Taylor, J. R., Ferrari, R., & Joyce, T. M. (2013). Symmetric instability in the
786 Gulf Stream. *Deep Sea Research Part II: Topical Studies in Oceanography*, *91*, 96-110.
787 doi:10.1016/j.dsr2.2013.02.025

788 Thompson, A. F., Lazar, A., Buckingham, C., Naveira Garabato, A. C., Damerell, G. M., &
789 Heywood, K. J. (2016). Open-ocean submesoscale motions: A full seasonal cycle of mixed layer
790 instabilities from gliders. *Journal of Physical Oceanography*, *46*(4), 1285-1307.
791 doi:10.1175/JPO-D-15-0170.1

792 Wenegrat, J. O., Thomas, L. N., Sundermeyer, M. A., Taylor, J. R., D'Asaro, E. A., Klymak, J.
793 M., . . . Lee, C. M. (2020). Enhanced mixing across the gyre boundary at the Gulf Stream front.
794 *Proceedings of the National Academy of Sciences*. doi:10.1073/pnas.2005558117

795 Yu, X., Naveira Garabato, A. C., Martin, A. P., Buckingham, C. E., Brannigan, L., & Su, Z.
796 (2019). An annual cycle of submesoscale vertical flow and restratification in the upper ocean.
797 *Journal of Physical Oceanography*, *49*(6), 1439-1461. doi:10.1175/JPO-D-18-0253.1

798 Zhu, J. (2017). Descriptive analysis of frontal symmetric instabilities without background
799 temperature gradient. *Brown University*. http://www.geo.brown.edu/research/Fox-
800 Kemper/pubs/pdfs/Zhu17.pdf

801